James, Clancy William; Ekers, Ronald David; Alvarez Muñiz, Jamie; Bray, Justin D.; McFadden, R. A.; Phillips, C. J.; Protheroe, Raymond John; Roberts, P.
LUNASKA experiments using the Australia Telescope Compact Array to search for ultrahigh energy neutrinos and develop technology for the lunar Cherenkov technique
Physical Review D, 2010; 81(4):042003

http://link.aps.org/doi/10.1103/PhysRevD.81.042003

LUNASKA experiments using the Australia Telescope Compact Array to search for ultrahigh energy neutrinos and develop technology for the lunar Cherenkov technique

C. W. James,[1,*] R. D. Ekers,[2] J. Álvarez-Muñiz,[3] J. D. Bray,[1,2] R. A. McFadden,[4,2] C. J. Phillips,[2] R. J. Protheroe,[1] and P. Roberts[2]

[1]*School of Chemistry and Physics, University of Adelaide, Australia*
[2]*Australia Telescope National Facility, Epping, Australia*
[3]*Department Fisica de Particulas and IGFAE, Universidad de Santiago de Compostela, Spain*
[4]*School of Physics, Univ. of Melbourne, Australia*

(Received 16 November 2009; published 26 February 2010)

We describe the design, performance, sensitivity and results of our recent experiments using the Australia Telescope Compact Array (ATCA) for lunar Cherenkov observations with a very wide (600 MHz) bandwidth and nanosecond timing, including a limit on an isotropic neutrino flux. We also make a first estimate of the effects of small-scale surface roughness on the effective experimental aperture, finding that contrary to expectations, such roughness will act to increase the detectability of near-surface events over the neutrino energy-range at which our experiment is most sensitive (though distortions to the time-domain pulse profile may make identification more difficult). The aim of our ''Lunar UHE Neutrino Astrophysics using the Square Kilometre Array'' (LUNASKA) project is to develop the lunar Cherenkov technique of using terrestrial radio telescope arrays for ultrahigh energy (UHE) cosmic ray (CR) and neutrino detection, and, in particular, to prepare for using the Square Kilometre Array (SKA) and its pathfinders such as the Australian SKA Pathfinder (ASKAP) and the Low Frequency Array (LOFAR) for lunar Cherenkov experiments.

DOI: 10.1103/PhysRevD.81.042003 PACS numbers: 98.70.Sa

I. INTRODUCTION

The origin of the ultrahigh energy cosmic rays (UHE CR)—protons and atomic nuclei with observed energies above 10^{18} eV and up to at least 2×10^{20} eV—is obscured due to their deflection and scattering in cosmic magnetic fields. This makes the flux of all but the highest energy CR appear almost isotropic with respect to the Galaxy regardless of their source, so that measurements of arrival directions cannot reliably be used for source identification. At the highest energies, the deflection is less, and this allows the possibility of ''seeing'' nearby UHE CR sources. Arrival directions of UHE CR detected by the Pierre Auger experiment above 5.6×10^{19} eV are found to be statistically correlated with positions of nearby active galactic nuclei (AGN), which are in turn representative of the large-scale distribution of matter in the local universe [1]. However, the flux is extremely low, and so the nature of the sources of UHE CR within this distribution remains at present unresolved.

An alternative means of exploring the origin of UHE CR is to search for UHE neutrinos. As first noted by Greisen [2] and by Zatsepin and Kuzmin [3], cosmic rays of sufficient energy will interact (e.g. via pion photoproduction) with photons of the 2.725 K CMB, with the resulting energy-loss producing a cutoff in the spectrum (the 'GZK cutoff') at around $\sim 10^{20}$ eV from a distant source. These same interactions produce neutrinos from the decay of unstable secondaries. Several experiments [4–9] have reported UHE CR events with energies above 10^{20} eV, and therefore a flux of these ''cosmogenic neutrinos'' is almost guaranteed.

Significant information on the CR spectrum at the sources is expected to be preserved in the spectrum of astrophysical neutrinos [10] which varies significantly between different scenarios of UHE CR production. These include acceleration in the giant radio lobes of AGN, the decay of supermassive dark matter particles or topological defects, and *Z*-burst scenarios, the last of which have already been ruled out by limits placed on an isotropic flux of UHE neutrinos [11,12]. Of course, neutrinos are not deflected by magnetic fields, and so should point back to where they were produced, with even a single detection allowing the possibility of identifying the source of UHE CR. Here we emphasize that in all models of UHE CR origin we expect a flux of UHE neutrinos. See Refs. [13,14] for recent reviews of UHE CR production scenarios and radio techniques for high-energy cosmic ray and neutrino astrophysics.

The lunar Cherenkov technique

A high-energy particle interacting in a dense medium will produce a cascade of secondary particles which develops an excess negative charge by entrainment of electrons from the surrounding material and positron annihilation in flight. The charge excess is roughly proportional to the number of particles in electromagnetic cascades, which in turn is roughly proportional to the energy deposited by the

*IMAPP, Radboud Universiteit Nijmegen, The Netherlands

cascade. Askaryan [15] first noted this effect and predicted coherent Cherenkov emission in dense dielectric media at radio and microwave frequencies where the wavelength is comparable to the dimensions of the shower. At wavelengths comparable to the width of the shower, the coherent emission is in a narrow cone about the Cherenkov angle $\theta_C = \cos^{-1}(1/n)$ (n is the refractive index), while for wavelengths comparable to the shower length, the coherent emission is nearly isotropic. The Askaryan effect has now been experimentally confirmed in a variety of media [16–18], with measurements of the radiated spectrum agreeing with theoretical predictions (e.g. Ref. [19]). If the interaction medium is transparent to radio waves, the radiation can readily escape from the medium and be detected remotely. Since the power in coherent Cherenkov emission is proportional to the square of the charge excess, i.e. to the square of the energy deposited, extremely high-energy showers should be detectable at very large distances.

The lunar Cherenkov technique, first proposed by Dagkesamanskij and Zheleznykh [20], aims to utilize the outer layers of the Moon (nominally the regolith, a sandy layer of ejecta covering the Moon to a depth of $\sim$10 m) as a suitable medium to observe the Askaryan effect. Since the regolith is transparent at radio frequencies, coherent Cherenkov emission from sufficiently high-energy particle interactions (specifically, from UHE cosmic ray and neutrino interactions) in the regolith should be detectable by Earth-based radio-telescopes (Askaryan's original idea was to place detectors on the lunar surface itself). First attempted by Hankins, Ekers, and O'Sullivan [21,22] using the Parkes radio telescope, the Goldstone Lunar UHE neutrino Experiment (GLUE) at the Goldstone Deep Space Communications Complex [11], the experiment at Kalyazin [23], and the NuMoon [24] experiment at the Westerbork Synthesis Radio Telescope (WSRT) have subsequently placed limits on an isotropic flux of UHE neutrinos. Our own project, LUNASKA, aims to develop the lunar Cherenkov technique for future use of the SKA. Observations continue at both WSRT [25] and with our own project using the ATCA and using the Parkes radio telescope (to be reported elsewhere). The technique has been the subject of several theoretical and Monte Carlo studies [19,26–29] together with our own recent work [22,30,31].

Future radio instruments will provide large aperture array (AA) tile clusters and arrays of small dishes with very broad bandwidths, with both factors allowing very strong discrimination against terrestrial radio frequency interference (RFI). The culmination of the next generation of radio instruments will be the Square Kilometre Array, to be completed around 2020, with smaller pathfinders such as ASKAP (Australian SKA Pathfinder [32]) to be built in the intervening period. In the meantime, we have been performing a series of experiments with the Australia Telescope Compact Array [33], an array of six 22 m dishes which were undergoing an upgrade to an eventual 2 GHz bandwidth at the time of the observations described here. Lunar Cherenkov experiments with these instruments, together with those proposed for LOFAR [25], represent the foreseeable future of the technique. We emphasize that the lunar Cherenkov technique is very different to conventional radio astronomy and requires nonstandard hardware and signal processing as it is necessary to detect nanosecond-duration lunar Cherenkov radio pulses coming from a region too large (the apparent diameter of the Moon is 0.5°) to image in conventional ways at nanosecond time resolution. Such pulses suffer dispersion in the Earth's ionosphere, and our experiment is the first to correct for this in real-time.

In the present paper we describe our recent experiments using the ATCA using the lunar Cherenkov technique. We start by giving an overview of the experiment, the part of the moon targeted and observing times which were chosen in order to observe the Galactic Center and Centaurus A (UHE neutrino flux limits for these sources are reported in Ref. [34]), the antennas used, specialized hardware, triggering and signal processing. We then discuss the effects of dead-time, our finite sampling rate and our approximate de-dispersion on the detection efficiency and effective observation time. Finally, we present a new limit to an isotropic UHE neutrino flux, and discuss why it is important despite better limits existing from the Antarctic Impulsive Transient Antenna (ANITA) and the Radio Ice Cherenkov Experiment (RICE). In appendices, we outline the effects of the two major theoretical uncertainties in our aperture and limit calculation being the UHE neutrino cross-section, and the small-scale lunar surface roughness. In the latter case, a new approximate treatment is described, which we use as well as the standard calculation methods to determine the experimental apertures and limits given in the main body of the paper.

II. DESCRIPTION OF THE EXPERIMENT

The Australia Telescope Compact Array (ATCA—see Fig. 1) is an aperture synthesis telescope located at latitude $-30°$ near Narrabri, NSW, Australia. It consists of six identical 22 m dishes. One antenna is fixed in position, while the other five can be moved along a 3 km East-West baseline, and also a $\sim$150 m North-South baseline. We used three of the moveable dishes on the East-West baseline for our observations and used triple coincidences with the correct relative timing to identify pulses coming from the direction of the Moon

The ATCA was chosen as an ideal SKA test-bed for the lunar Cherenkov technique because: the antennas have a size comparable to that expected for the SKA; the beam-size matches the lunar disk at 1 GHz; it provided us with 600 MHz of bandwidth (to be upgraded to 2 GHz); because it is an array it provides strong timing discrimination against terrestrial RFI; and because it can give a large

FIG. 1. A photograph of three of the six ATCA antennas. For the observations described here, the distance between the antennas was greater.

aperture sensitivity while seeing the entire moon [35]. Full details of the experiment and observations are given by James [36].

A. Observations

The observations described here cover two observing periods: February and May 2008, all at the ATCA. Table I specifies the array configuration used in each observation period. The baselines used were a compromise between baselines long enough to resolve correlated thermal emission from the Moon, and short baselines to reduce the search window in the time domain for pulses coming from any location on the Moon. For these initial observations we implemented our special hardware on only three of the ATCA antennas: CA01, CA03, and CA05.

Observation times and antenna pointings

We had two main considerations in choosing our observation times, the first being to confine the observations to within the approximate hours of 10 pm to 6 am, in order to have a stable ionosphere (see Sec. II D 1). The requirement of the Moon being visible meant that this gave us a window of perhaps five days in every 29.5-day synodic lunar month where the Moon would be sufficiently visible during this period to warrant observations. The second requirement was that the Moon be within $\sim 35°$ of particular regions of sky of interest [31]. This occurs once per 27.3-day lunar orbit for any given region, so that combined, we typically had three good and two marginal periods of a few nights each year in which to observe any given source.

The February 2008 run was tailored to ''target'' a broad ($\gtrsim 20°$) region of the sky near the Galactic Center, harbouring the closest supermassive black hole to Earth, and a potential accelerator of UHE CR. The Galactic Center may also be a source of UHE CR and neutrinos through the decay of massive particles in its dark matter halo (see [37] and references therein). Preliminary calculations showed that for beam-sizes similar to that of the ATCA, the greatest total effective aperture (and hence sensitivity to an isotropic or very broadly-distributed flux) is achieved when pointing the antennas at the center of the Moon, so all the limb is at approximately the half power point of the antenna beam. Since any UHE neutrino flux from this region is likely to be broadly-distributed, we used this pointing for these runs. Our May 2008 observing period targeted Centaurus A only, the nearest active galaxy which could potentially account for some of the UHE CR events observed by the Pierre Auger observatory [1], and to achieve the maximum sensitivity to UHE neutrinos from this source we pointed towards the portion of the lunar limb closest to Centaurus A so it is observed at full sensitivity.

B. Specialized hardware

The background signal above which any genuine nanosecond-duration lunar Cherenkov pulses had to be detected consisted of two components: random noise fluctuations, mainly thermal emission from the lunar disk and to a lesser extent system noise and Galactic plane synchrotron emission; and man-made RFI. Figure 2 gives a diagram of the hardware and signal path at each antenna. In order to perform a search for short-duration lunar pulses, against a background of thermal noise fluctuations and RFI, we had to build specialized hardware to detect and store candidate events in real time. For this we used the digital, field-programmable gate array (FPGA) based analog-to-digital converters (ADC) used in the Compact Array Broad Band (CABB) upgrade [38], each of which could digitize and perform simple logic on two data streams at a rate of 2.048 GHz. As well as this, we required specialized software running on the control room com-

TABLE I. Positions of the antennas used during the LUNASKA lunar observations, and the baselines.

Date	Configuration	Antenna stations			Baselines (m)		
		CA01	CA03	CA05	1–3	1–5	3–5
Feb 26–28 2008	750B	W98	W113	W148	230	766	536
May 18 2008	750A	W147	W172	W195	383	735	352
May 19 2008	EW352	W102	W109	W125	107	352	245

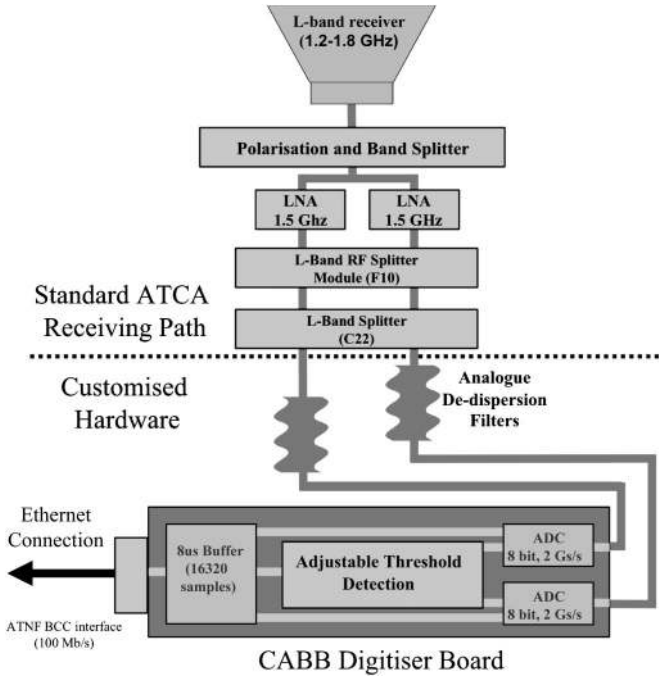

FIG. 2. Diagram of the signal path at each antenna. Abbreviations are: ''LNA'': low noise amplifier, ''ADC'': analogue–digital converter.

puters to interface with the CABB analog-to-digital converter boards, and a hardware method to correct for the dispersive effects of the Earth's ionosphere.

1. Data channels and signal path

During each observation period, the received signal—split into two orthogonal linear polarizations, which we arbitrarily label ''A'' and ''B''—was processed by our specialized hardware at each of three antennas, providing a total of six output data streams. By connecting to a monitor point at the receivers in each antenna we bypassed the normal narrow-band ATCA intermediate frequency (IF) system and obtained a nominal bandwidth of 600 MHz between 1.2 and 1.8 GHz. For May 2008 a high-pass filter was added to remove a strong 0.9 GHz (aliased to 1.1 GHz) narrow-bandwidth RFI from a known transmitter which was perturbing our detection threshold.

Each polarized data stream was fed through an analog de-dispersion filter before being sampled by a CABB analog–digital converter board. This operated at 2.048 Gs/s with 8-bit effective precision. Since both the 100 Mb/s connection from each antenna to the central control room (where all antenna signals could be combined) and the CABB correlator architecture were inadequate to handle the full raw data rate of $2 \times 8 \times 2048$ megabit/s per antenna, we had to reduce our data volume by triggering independently at each antenna and returning only blocks of data containing candidate events. The signal was copied into both a running buffer and passed to a real-time trigger algorithm, and on fulfilling the trigger conditions a portion of the buffer was returned to the control room and recorded. During this recording process, the buffer was unable to respond to further triggers, and the experiment was temporarily blind to any events. The period of this dead-time depended on the length of the buffer to be returned.

2. Trigger logic and levels

The trigger algorithm was set up to be a simple threshold trigger at each antenna—if the square of any single sample on either the A or B polarization data streams was above a certain value, both polarizations were returned. The thresholds were adjusted occasionally to keep the trigger rates on each receiver output constant at approximately 40–50 Hz corresponding to $\sim 5\sigma$, where we use σ as shorthand for the rms voltage $V_{\rm rms}$ in the output channel. Even with our 8-bit sampling we were barely able to adjust these threshold with sufficient precision ($< 0.1\sigma$ increments) while maintaining a reasonable dynamic range for any detected event. The gain was adjusted to give an RMS sampler output of approximately 10 ADC digitization units (a.d.u.) and hence a maximum of 12.8σ (128 a.d.u) before saturation for an 8-bit signal.

C. Dead-time and efficiency

A certain degree of dead-time loss is suffered for every trigger. As all three antennas need to be ''on'' to record an event, it is important to avoid setting the thresholds too low (trigger rates too high) as this can make the effective observation time negligible. This dead-time can be easily measured by setting the thresholds to zero and recording the maximum trigger rate for a given buffer length. Such measurements were performed at each observation period, and the results are recorded in Table II. We see that for a buffer length of 256 samples the dead-time per trigger was approximately 1 ms.

The efficiency of the experiment can be defined as the time-fraction when all three antennas are sampling and ready to trigger. For a sampling rate r_i (Hz) on antenna i, maximum rate R_i, and purely random trigger events, the efficiency ξ is given by:

$$\xi = \Pi_i \left(1 - \frac{r_i}{R_i}\right), \tag{1}$$

where the i multiplies over all three antennas. In Fig. 3 we plot the trigger rates for all antennas for the 18 May 2008 observations and the efficiency ξ calculated as in Eq. (1), assuming a constant $R_i = 1040$ from Table II corresponding to our buffer length of 256 samples. A short-duration burst of RFI is evident at UT 12:50 in Fig. 3, as is a large increase in the background between UT 15:00 and UT 17:00. During these periods of intense RFI the efficiency (upper dashed line) is significantly reduced. The effective observation time $t_{\rm eff}$ was determined by integrating the

TABLE II. Maximum trigger rates (Hz) as a function of buffer length for 18 May 2008.

Buffer length	16256	8192	4096	2048	1028	512	256	128	64
Trigger rate	22	42	83	163.5	317.5	581	1040	1690	2450

efficiency over the observation time $t_{\rm obs}$, and this is given in Table III together with the average efficiency $\bar{\xi} = t_{\rm eff}/t_{\rm obs}$.

D. Ionospheric dispersion

For our experimental bandwidth of 600 MHz centered at 1.5 GHz, the effects of dispersion in the Earth's ionosphere are significant. The dispersion is due to a frequency-dependent refractive index caused by free (ionized) electrons in the ionosphere. Using the standard measure for the number of electrons (total electron content units, or TECU: $10^{16} e^-/\mathrm{cm}^2$), the time-delay δt relative to a vacuum for a frequency ν is given by Eq. (2):

$$\delta t = 1.34 \times 10^{-7}\,\mathrm{TECU}\,\nu^{-2}. \quad (2)$$

Of more use is the dispersion Δt over a bandwidth $\Delta\nu$, given by

$$\Delta t = 1.34 \times 10^{-7}\,\mathrm{TECU}(\nu_{\rm min}^{-2} - \nu_{\rm max}^{-2}) \quad (3)$$

$$\Delta t \approx 2.68 \times 10^{-7}\,\mathrm{TECU}\,\Delta\nu\,\bar{\nu}^{-3} \quad (4)$$

if $\Delta\nu \ll \bar{\nu}$, where $\bar{\nu}$ is the mean frequency $(\nu_{\rm min} + \nu_{\rm max})/2$. Note that in terms of phase delay, the correction goes as $\bar{\nu}^{-2}$.

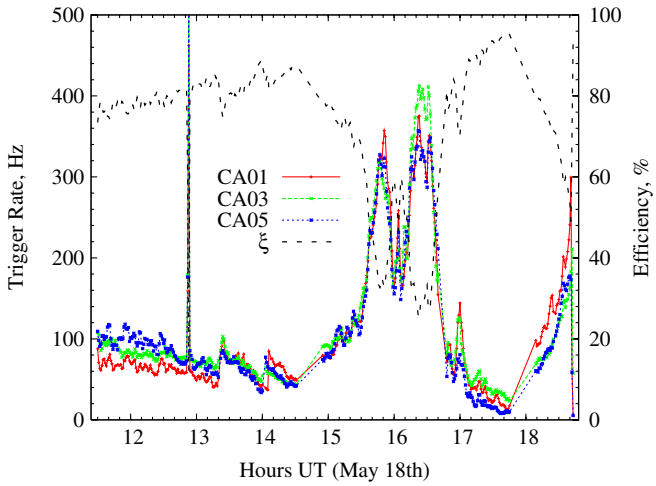

FIG. 3 (color online). Trigger rates for the three antennas (three lower curves) and efficiency (upper curve) from Eq. (1) for the night of May 18th, 2008. The increased trigger rate at UT 15:00–17:00 results from a "Type 1" noise feature caused by an unknown source—see Sec. V and the top-center of Fig. 10.

TABLE III. Raw observation time $t_{\rm obs}$ (minutes), mean efficiency $\bar{\xi}$ (%), and effective observation time $t_{\rm eff}$ (minutes), for all observation periods.

Date	$t_{\rm obs}$	$\bar{\xi}$	$t_{\rm eff}$
26 Feb. 2008	239	86	204
27 Feb. 2008	319	87	277
28 Feb. 2008	314	87	274
17 May 2008	324	69	224
18 May 2008	376	73	274
19 May 2008	440	72	316

De-dispersion filters

Implementing a digital de-dispersion filter running at this speed was too difficult at the time, so we used analog de-dispersion filters designed by Roberts [39]. Each filter was a variable-width waveguide of approximately one meter in length constructed as a spiral for compactness (Fig. 4), with the output being the continuous sum of reflections along the length. Upon reflection, high frequencies experienced a greater delay than low frequencies, with the design such that this cancelled out the delay due to ionospheric dispersion at low frequencies. Thus an in-phase signal (e.g. coherent Cherenkov radiation from a

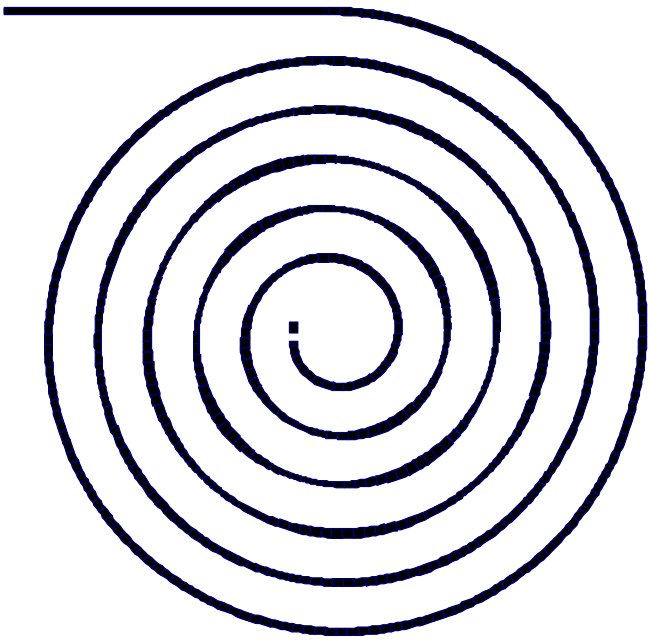

FIG. 4 (color online). Printed circuit board layout of analog dedispersion filter. Note the variation in the width of the waveguide along its length. The physical size is approximately 25 × 25 cm.

UHE particle interaction in the Moon) entering the top of the ionosphere should appear in-phase after de-dispersion, provided the correct dispersion measure was used.

We used NASA data [40] to predict typical values of the ionospheric dispersion at Narrabri, with results reported in Ref. [41]. Since we were still near solar minimum these results showed that the ionosphere over Narrabri was comparatively stable between the hours of 10 pm and 6 am, with low and predictable vertical total electron content (VTEC) measures around 7 ± 1.3 TECU. This corresponds to a differential vertical delay of 3.6 ns over a 1.2–1.8 GHz bandwidth. Since the actual delay will depend on the slant angle, we chose to build the filters assuming a 5 ns delay over the band, i.e. a TEC along the line of sight (slant TEC, or STEC) of 10 TECU; this is also equivalent to the mean VTEC of 7 TECU with a lunar elevation of 47°. Therefore we expected to lose some sensitivity when the Moon was directly overhead, and also very near the horizon. The sensitivity lost due to deviations of the actual VTEC from the mean and variations in lunar elevation is discussed in Sec. III. Figure 5(a) shows the expected effect

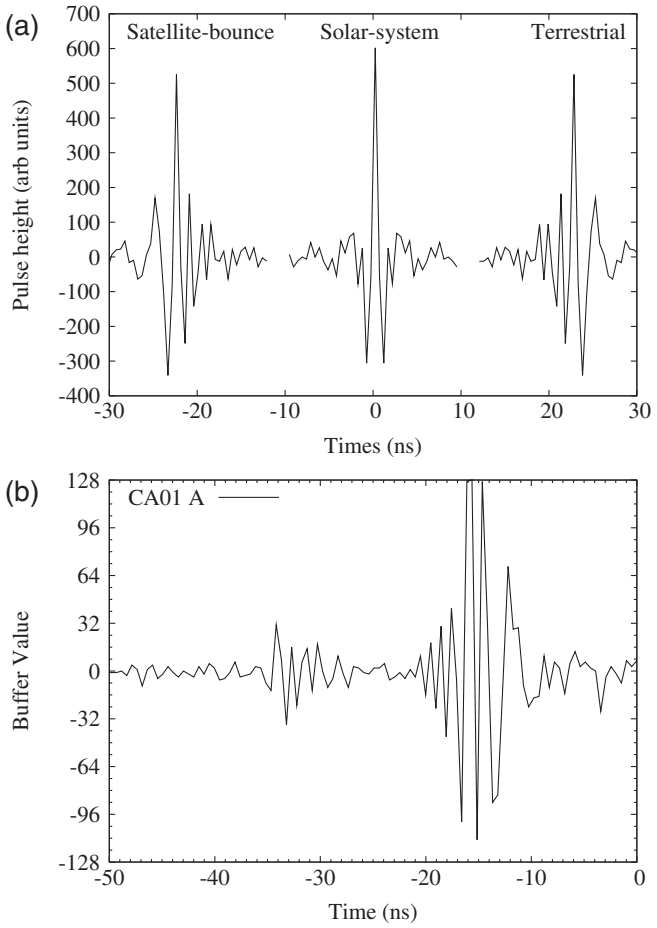

FIG. 5. (a) Predictions of an observed impulse of different origins. (b) A typical noise-calibration pulse—in this case, from CA01 A on Feb 26th. The small prepulse at −35 ns is caused by a spurious reflection from the filter connection point.

of dedispersion on pulses of different origin: satellite bounce (of RFI), solar system (lunar Cherenkov) and terrestrial (RFI). These have been modeled, respectively, as a flat frequency spectrum dispersed once (dispersed twice then de-dispersed once), a ν^2 spectrum expected for coherent Cherenkov emission unchanged (dispersed once then de-dispersed once), and a flat frequency spectrum de-dispersed once. In all cases the Fourier inverse has been taken over 1.2–1.8 GHz, i.e. the pulse has been band-limited to 1.2–1.8 GHz.

E. The noise diode

A noise-calibration diode is located in the receiver and used to calibrate the power through measuring the system temperature, T_{sys}, during normal ATCA observations. During testing, we observed unexpected strong pulses at a rate of approximately 8 Hz [Fig. 5(b)]. It was discovered that these pulses were generated by the switching of the noise-calibration diode. Note that, as expected, the pulse in Fig. 5(b) closely resembles that expected for a terrestrial source.

Since the noise diode could be turned on and off from the control room, it could be used to generate approximately coincident false triggers between the three antennas. The time difference in the noise diode switching between antennas was small (< 1 μs) and the scatter about this offset was $\sim$200 ns. Using this simple procedure to generate approximately coincident false triggers became a useful part of our experimental procedure as discussed in Section .

III. SAMPLING AND DISPERSIVE EFFECTS ON SENSITIVITY

The effects of loss of sensitivity due to a finite sampling rate (compared to an infinite sampling rate) and dedispersion depend on the frequency spectrum of the radio pulse and the bandwidth of the detector. The expected lunar Cherenkov pulse spectrum depends on many factors, including lunar surface-roughness and orientation, the dimensions and direction of the electromagnetic cascade in the lunar regolith, and on the neutrino energy—these are discussed in detail elsewhere [30]. The range of possible spectra is very broad. However, for our purposes we consider two extreme cases. We are concerned with the relative strengths of the high-frequency and low-frequency components. Near the minimum detectable cascade energy for our experiment (10^{20} eV—see Sec. 15), only fully coherent emission will be detectable. The electric field spectrum (V/m/MHz) will therefore have the form $E(\nu) = A\nu$, which gives the greatest possible weight to the high-frequency component.

The other extreme is given by a high-energy shower, at shallow depth and viewed at a large angle away from the Cherenkov angle where the emission from the cascade is becoming incoherent. In this case we expect

$E(\nu) = B\nu \exp(-C\nu^2)$ based on approximate fits to the spectrum far from the Cherenkov angle for hadronic showers [42]. For any observed pulse of given total power we do not know the shape of the spectrum to expect if the pulse is indeed of lunar origin, and so we consider the two extreme possibilities. For our "high-energy" we take 10^{23} eV, since above this range strong limits on a neutrino flux from the NuMoon [24] and FORTE [43] experiments made a detection extremely unlikely. For the same reasons, 10^{23} eV is also the most energetic neutrinos to which we simulate our effective apertures and limit, which can at most produce cascades of energy 10^{23} eV. Setting the peak power in the bandwidth to be the same for the two extreme cases, corresponding to 10^{20} eV and 10^{23} eV neutrinos, and taking $B/A = (10^{23}/10^{20})$ allows the constant C to be found as follows. Since the electric field of a pulse (wave packet) at the antenna may be written as

$$E(t) = \int_{-\infty}^{\infty} E(\nu) e^{2\pi i \nu (t - t_0)} d\nu, \tag{5}$$

and since the power is proportional to $|E(t)|^2$, the peak power occurs at $t = t_0$ and so is proportional to

$$|E(t_0)|^2 = \left| \int_{-\infty}^{\infty} E(\nu) d\nu \right|^2. \tag{6}$$

Hence, for equal peak powers for the two extreme forms of possible spectra we may solve

$$A \int_{\nu_1}^{\nu_2} \nu d\nu = B \int_{\nu_1}^{\nu_2} \nu \exp(-C\nu^2) d\nu. \tag{7}$$

For $B/A = 10^3$, $\nu_1 = 1.2$ GHz, and $\nu_2 = 1.8$ GHz we find $C = 3.515$ GHz^{-2}. We shall use these results when finding the uncertainty in sensitivity due to the unknown spectral shape.

A. The effects of a finite sampling rate only

Our sampling rate of 2.048 Gs/s was greater than the Nyquist rate of 1.2 Gs/s for our nominal 600 MHz bandwidth, and allowed for perfect reconstruction of the signal in the frequency range 1.024 to 2.048 GHz at arbitrary time resolution (assuming no signals outside this range). However, experiments (such as this one at the ATCA) which are pushing the current FPGA limits for high-speed signal processing can only use simple algorithms based on the pulse height of a single sample as captured by the sampling threshold. For any finite sampling rate (including the Nyquist rate), there will be a random offset in the phase of the ADC digitization times between the actual peak of the pulse and the sampling times. Figure 6 plots the peak pulse height as a function of the arbitrary phase offset for the sampling rate of 2.048 Gs/s as used in our experiment and the two extreme spectra of lunar Cherenkov emission. The peak sampled value is seen to vary by ~30% in the case where the Cherenkov emission is fully coherent, and by ~15% when the emission is becoming incoherent. Hence, with our simple trigger logic, there will be a triggering inefficiency due to our finite sampling rate causing the peak sampled voltage occasionally to be less than the trigger level, even if the actual peak voltage in a pulse was above it. In future experiments, we will use a more complex trigger algorithm which works off multiple sampled values in order to reduce this loss, which is a more efficient remedy than increasing the sampling rate.

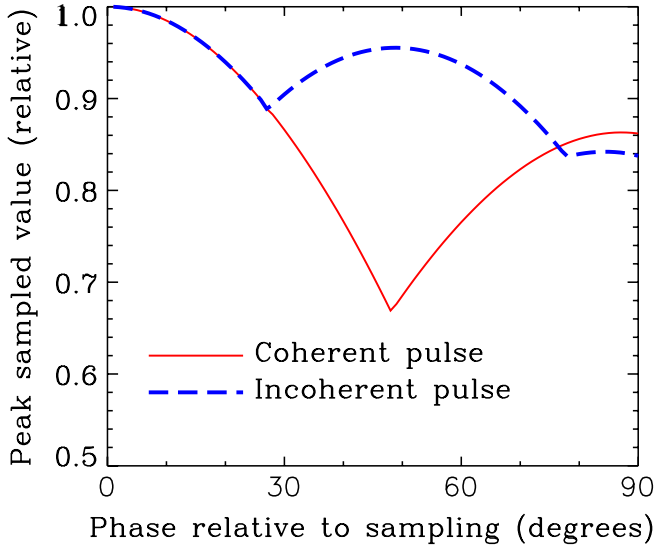

FIG. 6 (color online). (color online) Maximum sampled value as a fraction of the true pulse height as a function of the arbitrary phase offset for sampling rate of 2.048 Gs/s and two extreme lunar Cherenkov pulse types.

B. Effects due to dedispersion

In order to quantify the effect of using the constant TEC value built into our dedispersion filters, we take pulses of the two extreme types discussed above, disperse them for different line-of-sight TEC values, dedisperse them using the constant TEC value built into our dedispersion filters, and finally simulate sampling by the ADC. All possible offsets of the pulse-peak arrival time with respect to the sampling times, or "base phase offsets", were modeled in this process. For each combination of intrinsic spectrum, base phase offset, and dispersion measure, we calculate the peak pulse strength in the time domain. Averaging this over all base phase offsets (which will be random) and dividing by the magnitude of the peak undispersed pulse at zero phase offset we obtain the peak signal strength as a function of line-of-sight TEC shown in Fig. 7. As well as the sampling rate of 2048 GHz used, we also show results for sampling rates a factor of 2 higher and lower. The upper and lower sets of lines are for pulses due to incoherent and coherent Cherenkov emission by the lunar cascade as a whole, respectively. The pulse for fully-coherent Cherenkov radiation is most adversely affected by iono-

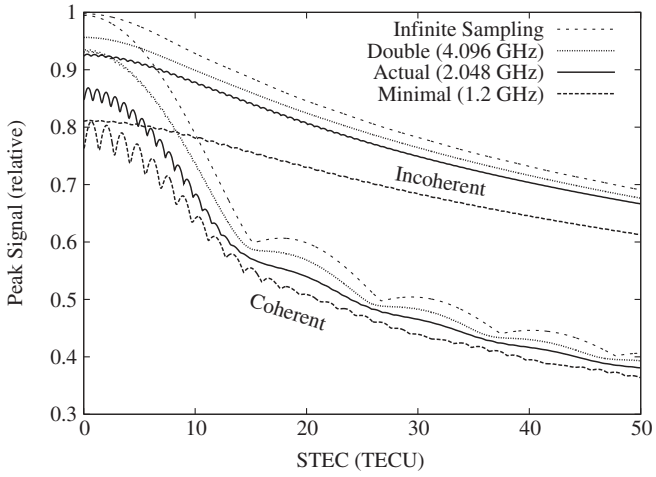

FIG. 7. Greatest detected amplitude of the time-domain signal relative to the maximum undispersed amplitude, for two extreme lunar Cherenkov pulse types and four sampling rates, as a function of the difference between the line-of-sight total electron content, in TECU, and the constant value used in the dedispersion.

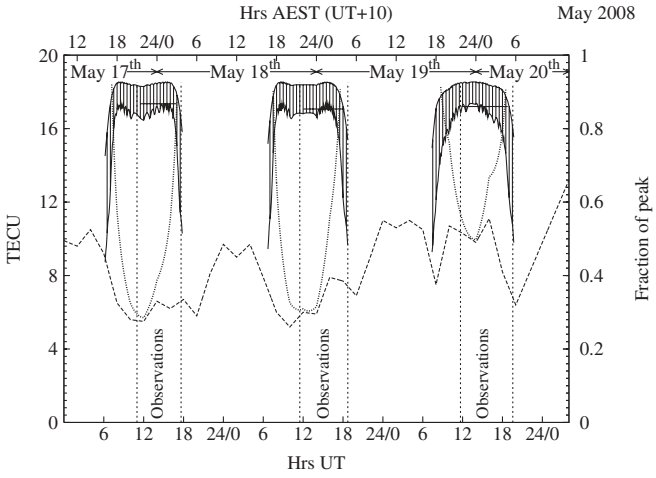

FIG. 8. Ionospheric influence over our May 2008 observations. Dashed curves: measured VTEC (TECU) from Ref. [40]. Dotted curves: STEC (slant TEC along the line-of-sight). Solid curves: mean fractional loss for coherent (lower curve) and incoherent (upper curve) lunar Cherenkov pulses due to ionospheric effects and triggering inefficiency due to our noninfinite sampling rate (see Fig. 6): the shading gives the range. Vertical lines indicate the times of the observations, horizontal lines give the fractional loss averaged over each observation and over the two extreme cases for the expected spectrum.

spheric dispersion because the signal is spread over the largest frequency range. The rapid oscillations in average peak amplitude with changing line-of-sight TEC for the coherent Cherenkov pulse is due to the combined effect of the sharp band edges and the dedispersion function. The mean values from Fig. 6 correspond to zero line-of-sight TEC for the case of a 2048 GHz sampling rate, allowing a comparison between the effects of our finite sampling rate and dispersion. We note that the loss in sensitivity due to errors caused by using a constant TEC value for dedispersion (typically differing from the true value by less than 4 TECU) are less than the finite sampling rate errors for our observations using a simple trigger algorithm.

C. Loss of experimental sensitivity

The loss of sensitivity due to sampling and dispersive effects can be calculated using the measured values of total electron content (TEC) as a function of elevation, which were determined after the observations [40]. The results are given in Fig. 8. Using a linear interpolation between these points and the known lunar elevation gives the line-of-sight TEC (slant TEC, or STEC) measure (dotted lines). At low elevations, the line-of-sight will probe a large horizontal distance, so using a constant VTEC measure may not be appropriate. However, since the TEC goes as $1/\sin(\text{elevation})$ and consequently blows up at low elevations, the sensitivity in this regime will be low in any case. Combined with the mean losses for the two spectra in Fig. 7, the range of losses for the experimental periods is calculated as the shaded regions in Fig. 8 which are bounded by the extreme spectra of coherent/incoherent lunar Cherenkov emission by lunar cascades.

TABLE IV. Estimated nightly average fractions of the peak signal detected (%) for the observations periods indicated. The best case corresponds to incoherent Cherenkov emission from lunar cascades, the worst case to completely coherent lunar Cherenkov emission signals, as discussed in text.

Period	February 2008				May 2008			
Date	26th	27th	28th	Mean	17th	18th	19th	Mean
Best (%)	92	91	91	91	91	91	91	91
Worst (%)	84	80	81	82	82	80	81	81
Mean (%)	88	86	86	87	87	86	86	86

The effect of using a fixed STEC value for the dedispersion is estimated by taking the mean loss over both observation time and spectral type, giving equal weighting to both the coherent and incoherent spectra. The resulting mean detected signal fractions are given in Table IV.

IV. RELATIVE TIMING CALIBRATION WITH ASTRONOMICAL POINT SOURCES AND RFI SOURCES

We had counters recording the number of samples at each antenna, the value of which was returned with each triggered event. These could be converted to clocks accurate to $\sim$0.5 ns. However, at the time of our experiment these clocks had unknown timing offsets between them, which had to be determined to allow a sufficiently rigorous pulse search. To calibrate the times, we required both a

common signal in each antenna with some known time-delay, and a method to trigger the buffers with sufficient simultaneity that enough of the common signal seen by all three antennas would be captured to produce a significant correlation. We used the noise-calibration pulses (see Sec. II E) as our trigger, and the very bright discrete radio sources 3C273 and 3C274 (M87) as our correlated signal.

The QSO 3C273 was chosen since it was the brightest (47 Jy at 1.4 GHz) pointlike source near the Moon at the time of the observations, and would thus give a strong correlation over all baselines. The radio galaxy M87 is brighter (215 Jy at 1.4 GHz) [33] but resolved on our long baselines, and was chosen to maximize the correlated signal over our shortest (CA01-CA03) baseline only.

Timing observations

To calibrate the timing, we pointed the antennas at either 3C273 or M87, set the buffer length to maximum, switched the noise-calibration on, and set the trigger thresholds such that we were triggering only off the noise-calibration pulses, at roughly 8 Hz. We typically observed in this calibration mode for a few minutes at a time and thus took of order 2000 pulses, repeating this procedure a few times each night.

The timing offsets, Δt, measured in samples, are given in Fig. 9 for the February observation periods. The vertical axis shows the absolute time offsets between antennas j and i, Δt^0_{ij}, relative to the first calibration after each clock reset—i.e. the first data points have been adjusted to 0. This adjustment is the timing calibration offset. The expectation was that all data would therefore have y-values near 0. Obviously this is not the case, and we see the time offsets Δt^0_{ij} jump around in multiples of 192 samples (93.75 ns).

We eventually discovered that these 192-sample offsets were a hardware fault triggered whenever we changed the buffer lengths. In the majority of cases we were able to use our logbook and RFI in the data to successfully identify when these offsets occurred and make the appropriate correction. In a small number of time blocks we still had ambiguity so we searched for event coincidences using all possible 192-sample offsets. Because the triple coincidence requirement is so strong this did not have an impact on the final sensitivity.

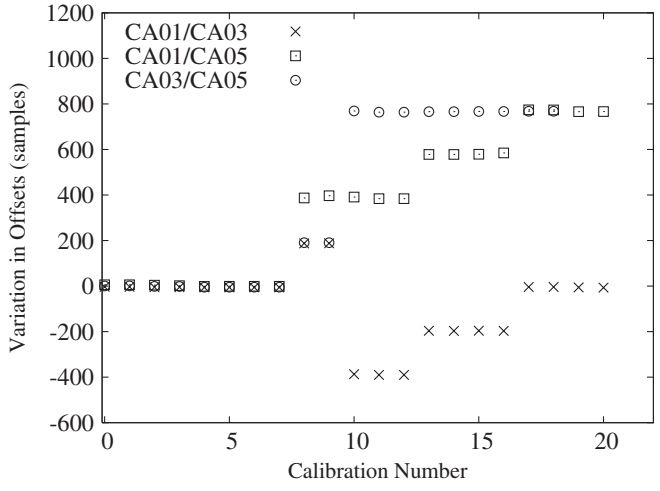

FIG. 9. Consistency check of correlation times in the February data: alignment relative to the first calibration of the February period, in (x-axis) chronological order.

V. RFI

After correcting the timing for the 192-sample jumps, we looked at coincident triggers within the physically possible time range for signals coming from outside the array. The number of twofold and threefold coincidences for each observation night are given in Table V. The most obvious result is the extremely large number of twofold coincidences, and the large number of threefold coincidences compared to twofold coincidences.

The expected rate (Hz) of twofold coincidences, R_{ij}, and threefold coincidences, R_{135}, from purely random arrival times is given by

$$R_{ij} = R_i R_j W_t \tag{8}$$

$$R_{135} = R_i R_j R_k W_t^2 \tag{9}$$

$$R_{135}/R_{ij} = R_k W_t. \tag{10}$$

where R_i is the rate (Hz) of single triggers in antenna i and W_t is the time window (seconds) required for a coincidence. Hence, the ratio between threefold and twofold coincidences increases with the trigger rate. For a maximum trigger rate R_i of 3 kHz and time-window $W_t = \pm 3.906 \times 10^{-6}$ s (8000 samples), the twofold rate is 70 Hz. However, the threefold rate is only 1.6 Hz, i.e. only $\sim$2% of the twofold rate. While at times the ratio of twofold to threefold coincidences matched this expectation exactly, there were also some periods within each night where up to 90% of coincidences between CA01 and CA05 were also coincident with a CA03 event, indicating an RFI source. The obvious conclusion therefore is that the vast majority of observed threefold coincidences do not occur purely randomly, but rather are triggered from a common

TABLE V. Number of twofold and threefold coincidences, within an 8000 sample ($\sim 4\ \mu$s) window for each night (the count of twofold events also includes the threefold events).

Date	CA01/03	CA01/05	CA03/05	CA01/03/05
February 26	6445	1286	1533	449
February 27	68894	39898	43224	30051
February 28	23296	8590	11072	6781
May 17	2344	1925	1994	96
May 18	21774	19445	20635	3437
May 19	114383	74311	71313	57493

event with significant time-structure. By extension, there will be many such events seen only in two antennas, and the same must therefore apply to the twofold coincidences, of which there are (generally) many more.

In Fig. 10, we have plotted all twofold coincidences for each of the three pairs of antennas over the entire observing period for both runs—over 5×10^5 data points. For each twofold coincident event the angle, θ, between the East direction and the direction of propagation of a plane wave fitting the arrival times at the two relevant antennas is calculated, and $\cos\theta$ is plotted (dots) against the time of the occurrence of the event (top) February, and (bottom) May 2008. Time increases continuously except in breaks between days as indicated by the thick dashed vertical lines. Note that regions of high 'dot-density' appear blue only because the blue dots were plotted last. The lunar direction is indicated by the grey dotted line, and positions of candidate events (crosses) are marked. For May 17th, a network error necessitated many adjustments to the buffer size, resulting in multiple unknown timing offsets to occur during that night. Therefore the timing criteria for candidate lunar events have been relaxed to ± 5 sample offsets (i.e. ± 0.47 μs) on all antennas for May 17th, explaining why the four candidate events for that night do not lie exactly on the Moon's trajectory. For May 18 the trial offsets were ± 1 sample offsets (i.e. ± 94 nanoseconds) on all antennas, the system was more stable and had two calibrations in agreement, and on May 19 (and all of February) the times were completely aligned.

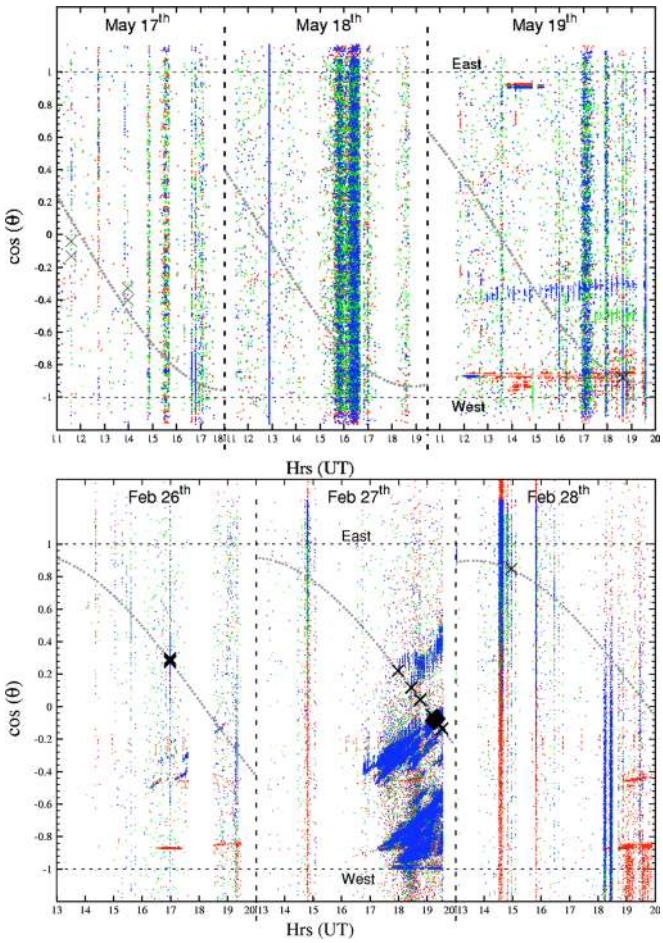

FIG. 10 (color online). For each twofold coincident event the angle, θ, between the East direction and the direction of propagation of a plane wave fitting the arrival times at the two relevant antennas is calculated, and $\cos\theta$ is plotted (dots) against the time of the occurrence of each event for February (top), and May (bottom). Red dots represent coincidences between antennas CA01 and CA03, green dots for CA01 and CA05, and blue dots for CA03 and CA05. In dot-dense regions, only blue points show, since they are plotted last. The lunar direction (grey dotted line) is also plotted, and positions of candidate events (crosses) are marked.

A stationary source of pulselike RFI producing triggers over a long period of time will show up as a horizontal line, while a very brief period of strong, narrow-band RFI will be observed as a very large number of coincidences over a small time range but large vertical extent (since the times will be random), i.e. a vertical line.

Figure 10 provides an amazing amount of information. The features can be approximately classed as below:

(1) Short time periods exhibiting a high rate of coincident triggers for all $\cos\theta$, mostly in May (e.g. 15:35 UT May 17th, 12:50 UT May 18th, 10:00–17:20 UT May 19th). These appear as vertical features which extend uniformly over the full range of offsets.

(2) Short time periods exhibiting a high rate of coincident triggers for a broad range of $\cos\theta$, mostly in February (e.g. 14:25 UT February 26th, 14:40 and 14:50 UT February 28th, and 19:40 UT May 19th). These appear as vertical features which do *not* extend over the full range of offsets.

(3) Purely horizontal, typically thin features occurring at a characteristic offset, sometimes over many days (e.g. the line at $\cos\theta = -0.88$ for 17:00 UT on February 26th and $\cos\theta = 0.92$ for 14:30 UT on May 19th.

(4) Sloped, typically broad features occurring most obviously around 17:00–19:00 UT on February 27th, but also on February 26th.

Type 1 features are exactly what would be expected from a high random trigger rate, with triggers evenly spread in time-offsets. The cause of the increased trigger rate must be a lowering of the effective threshold by an increase in the background containing no timing information, probably from narrow-band RFI—an increase due to ground temperature or the galactic background would be unlikely to produce such short-duration bursts. As would be expected, the triples rate is much lower than the doubles rate during these times, due to the random nature of the trigger times.

Type 2 features show both a small increase in triggers at all offsets corresponding to a random component from an

increased background, and a large increase in triggers spread about a specific offset. Some bands likely correspond to the nearby towns of Narrabri (East) and Wee Waa (West-Northwest) which present potentially large, extended sources of RFI. While these may be too weak to be detected under normal conditions, a decrease in the effective threshold due to the presence of narrow-band RFI could make such sources detectable. Another explanation is a single source of RFI with a broad time-structure, with a high likelihood of different antennas triggering off different parts of the signal, thereby adding a random component with a preferred direction. These features appear strongly for both doubles and triples, indicating the nonrandomness of the timing.

Type 3 features act exactly as fixed sources of short-duration RFI. The fixed geometrical delay results in a common time-offset regardless of antenna pointing position (and hence time).

Type 4 features remain largely unexplained. The locus of the coincident triggers (lines with constant slope) are consistent with some RFI source moving with constant speed in $\cos\theta$ (θ the angle w.r.t. the baseline), which is strong enough to give a high rate of triple-coincidences, and in the far-field, since the delays per unit baseline match. Since multiple features are seen at once, there must be either many such sources all moving in unison, or many multiple reflections keeping the same (and extremely large) angular offsets over a broad period of time. Also, the apparent motion is at the sidereal rate, but in the opposite direction. One suggestion is that a far-field RFI source is being observed over multiple signal paths due to tropospheric ducting which is associated with inversion layers. Reflections off the antennas themselves cannot explain the rate of change of delay being proportional to the baseline length, nor is the antenna size of 22 m sufficient to produce more than a $\sim$70 ns change in delays. We can be certain however it is not an equipment fault due to the presence of the aforementioned type 3 feature during this time period.

The apparent antisidereal motion of the features may result from either the real motion of far-field sources of RFI, or a series of reflections off an extended object, allowing each reflection point to move smoothly with time. In the former case, a possible candidate is a set of satellites in a medium Earth orbit (altitude $\sim$20, 000 km), which should move west-to-east across the sky at approximately the correct rate. This orbital altitude is occupied primarily by navigational satellites, such as those of the Global Positioning System (GPS), with ''L1'' and ''L2'' carrier frequencies of 1575.42 and 1227.6 MHz, respectively. The positions of the GPS satellites over the period of the experiment were checked from public ephemeris data [44], and found to exhibit the expected antisidereal motion, but they did not match the positions of the features. A more extensive search of all satellite positions might uncover a suitable candidate however.

Source identification with threefold triggers

If any on-site RFI sources are found, they could be deactivated and/or shielded in time for follow-up experiments, since in many cases these events dominate our trigger rates and limit sensitivity. Given three antenna positions on an East-West baseline, we can solve for the source position to within a North-South ambiguity, since an event some distance North of the baseline would produce exactly the same time structure if its location were directly South of the baseline by the same distance. We break the threefold coincidences into two types of events: near-field and far-field.

Using the timing offsets, a search for both far-field and near-field events was performed for each block of data in each of the February and May observation periods. The majority of near-field solutions occur in the very near-field (within 1 km of the antennas), and the rates of both near-field and far-field events are highly variable. In many cases pointlike sources of RFI are seen, both in the near-field and far-field, and it makes an interesting game trying to align the positions of possible RFI sources with those detected. Probable sources of RFI that we identified in this way include the residence, the control-building/lab, the solar observatory, the lodge, and either or both of the Ionospheric Prediction Service center or visitors center, all of which are on the ATNF site at Narrabri.

VI. SENSITIVITY CALIBRATION

To simulate the sensitivity of this experiment and place limits on a flux of UHE neutrinos, trigger levels at each antenna in terms of real quantities must be known. The usual specification for an experiment such as this is the detection threshold $E_{\rm thr}$ in V/m/MHz (a V/m threshold divided by the bandwidth) in a given polarization just prior to being received by the antenna. For instance, the GLUE threshold was a maximum field strength per bandwidth of $E_{\rm thr} = 1.23 \times 10^{-8}$ V/m/MHz, calculated by taking the threshold of 6.46×10^{-9} V/m/MHz in each circularly polarized data channel, and accounting for vacuum–receiver transmission and the splitting of power between polarizations [45]. To calculate our V/m/MHz threshold, we first had to perform our own calibration of the antenna gain as a function of frequency (bandpass calibration), since the automated ATCA measurement of $T_{\rm sys}$ using the injected noise source only applies to the standard signal path and over a small frequency range. Hence, another method had to be used, as described in the section below. Also discussed below are the effects of ionospheric dispersion, which while approximately corrected for, still reduced our sensitivity to some degree.

A. The calibration function $k(\nu)$

For a wideband experiment such as this, the signal is expected to change significantly in strength over the band.

Note that unless otherwise stated, $\Delta\nu$ refers to the total bandwidth from 1.024–2.048 GHz recorded, although the sensitivity outside the range 1.2–1.8 GHz will be minimal. Our sensitivity will change as a function of frequency due to the antenna, the receiver amplifier bandpass, and the dedispersion filter. Given that our threshold is set in terms of our 8-bit sampling, we need to be able to convert from a signal at the antenna resulting from coherent Cherenkov emission from a lunar cascade, $E(\nu)$ (V/m/MHz), to the value of the received buffer $b(t)$ at the peak of the pulse ($t = t_{\mathrm{peak}}$). From here on, we simply call the values of b ''ADC digitization units'', or ''a.d.u.'', and all frequencies are in units of MHz. The relationship between $E(\nu)$ and $b(t_{\mathrm{peak}})$ involves an unknown (but determinable) function $k(\nu)$, which is required to calculate the peak signal height (arbitrarily, occurring at time $t = 0$), defined as below:

$$b(t_{\mathrm{peak}})(\mathrm{a.d.u.}) = \int_{\nu_{\mathrm{min}}}^{\nu_{\mathrm{max}}} k(\nu)E(\nu)d\nu. \tag{11}$$

This gives the conversion between real field strength at the antennas and the measured units in the CABB ADC boards. For coherent pulses away from the peak, and for incoherent signals at all times, the integral on the right-hand side (rhs)of Eq. (11) should include a phase factor $e^{2\pi i\nu t}$, i.e. it is a Fourier transform. Therefore $k(\nu)$ can be more simply defined with respect to the Fourier transform $b(\nu)$ of $b(t)$ as per Eq. (12):

$$b(\nu) = k(\nu)E(\nu). \tag{12}$$

For simplicity, a more useful measure is $\bar{k}$, being the mean over the bandwidth $\Delta\nu$ between ν_{min} and ν_{max}:

$$\bar{k} = \frac{1}{\Delta\nu}\int_{\nu_{\mathrm{min}}}^{\nu_{\mathrm{max}}} k(\nu)d\nu. \tag{13}$$

The sensitivity of the experiment E_{thr}, defined in terms of a threshold electric field strength per unit bandwidth (for the simplest case of a flat-spectrum pulse), can then be calculated by knowing the trigger threshold b_{thr} using Eq. (14):

$$E_{\mathrm{thr}}(\nu)(\mathrm{V/m/MHz}) \approx \frac{b_{\mathrm{thr}}(t)}{\bar{k}\Delta\nu} \tag{14}$$

for $\Delta\nu$ in MHz. Therefore, in this section we calculate separately $k(\nu)$, $\bar{k}$, and hence E_{thr} for each data channel (antenna and polarization) over the entire observation period.

In order to calculate $k(\nu)$, a measurement of a known flux $F(\nu)$ (W/m^2/Hz) is required. For an incoherent signal (random phases), the relationship between $F(\nu)$ and the electric field over a given bandwidth is given by:

$$\int_{\nu_{\mathrm{min}}}^{\nu_{\mathrm{max}}} F(\nu)d\nu = E_{\mathrm{rms}}^2/Z_0, \tag{15}$$

where $Z_0 = \mu_0 c$ is the impedance of free space, and the RMS electric field is measured by the antenna system as:

$$E_{\mathrm{rms}}^2 = \frac{1}{\Delta t}\int_{t_{\mathrm{min}}}^{t_{\mathrm{max}}} E(t)^2 dt \tag{16}$$

Parseval's theorem for the $E(t) \leftrightarrow E(\nu)$ transform tells us that:

$$\int_{t_{\mathrm{min}}}^{t_{\mathrm{max}}} E(t)^2 dt = \int_{\nu_{\mathrm{min}}}^{\nu_{\mathrm{max}}} E(\nu)^2 d\nu. \tag{17}$$

Substituting Eq. (17) into (16), and then into Eq. (15), we arrive at Eq. (18):

$$\int_{\nu_{\mathrm{min}}}^{\nu_{\mathrm{max}}} F(\nu)d\nu = \frac{1}{Z_0\Delta t}\int_{\nu_{\mathrm{min}}}^{\nu_{\mathrm{max}}} E(\nu)^2 d\nu. \tag{18}$$

Since this relationship holds for an arbitrary bandwidth, the integration can be eliminated (e.g. let $\nu_{\mathrm{max}} \rightarrow \nu_{\mathrm{min}}$), giving:

$$F(\nu) = \frac{1}{Z_0\Delta t}E(\nu)^2. \tag{19}$$

Using Eqs. (11) and (19), the flux $F(\nu)$ as seen by the relevant data channel can then be related to the required calibration constant $k(\nu)$:

$$F(\nu) = \frac{1}{Z_0\Delta t}\left(\frac{b(\nu)}{k(\nu)}\right)^2 \tag{20}$$

which can be rearranged to give $k(\nu)$:

$$k(\nu) = \frac{b(\nu)}{\sqrt{F(\nu)Z_0\Delta t}}. \tag{21}$$

Equation (21) states that we can obtain $k(\nu)$ from a known flux $F(\nu)$ and the Fourier transform $b(\nu)$ of the corresponding sampled output. Note that the output is actually sampled discretely, so $b(\nu)$ is obtained indirectly, through a discrete Fourier transform. Note also that for incoherent thermal emission, we do not need to track the phase change in each antenna over the bandwidth, i.e. we are interested only in the magnitude of $k(\nu)$.

B. The Moon as a flux calibrator

For our calibrator, we chose the Moon. The lunar temperature T_M is stable to within a few degrees over the lunar cycle at approximately 225 K in the 1–2 GHz range (see Ref. [46]). There are small errors in this assumption due to the variation (1–2%) with lunar cycle, comparable variation across the band, and variations across the disk of the moon, and small polarization effects. Combining these errors, this method should be accurate to within 5% or better, which is acceptable.

Under these approximations, the lunar flux $F_M(\nu)$ (Jy) captured by the beam (it will be half this in any given polarization channel) is given by:

$$F_M(\nu) = \frac{2k_b T_M \nu^2}{c^2} \int_{\Omega_M} \mathcal{B}[\theta(\hat{\Omega}, \hat{\Omega}_p), \nu] d\Omega, \qquad (22)$$

where k_b IS the Boltzmann constant, and $\mathcal{B}(\theta, \nu)$ is the beam-power pattern of ATCA telescope dishes [47] at frequency ν at angle θ to the telescope pointing direction $\hat{\Omega}_p$, (i.e. θ is the angle between directions $\hat{\Omega}$ and $\hat{\Omega}_p$), and Ω_M is the solid angle subtended by the Moon. The beam-power pattern of ATCA deviates only slightly from the Airy pattern of a 22 m diameter aperture. In the present observations, $\hat{\Omega}_p$ was either the direction towards the center of the moon or towards the lunar limb.

C. Measurements

To obtain $b(\nu)$ by observing lunar thermal emission we took an unbiased sample of data pointing both on and off the Moon by setting the trigger level to zero, i.e. maximally triggering. The received flux $F_M(\nu)$ from the Moon can be detected by subtracting the measured bandpass $b_{\text{off}}(\nu)$ when pointing away from the Moon from the bandpass $b_{\text{on}}(\nu)$ when pointing at the Moon's center. The pointing-position for the off-Moon data was a position at similar galactic latitude far from any strong sources in the ATCA catalog. We set the buffer lengths to maximum for this procedure, since then the product of trigger rate and buffer length is largest, and also we obtain the best spectral resolution. This was done once every time the configuration was changed.

Each of the N_b recorded buffers was discrete-Fourier-transformed to produce $b(\nu)$ (typically $N_b \sim 5000$). The resulting spectra are squared and then averaged over all the buffers recorded for each calibration period/target taken. Each averaged spectrum is then cleaned with a very simple cleaning algorithm to remove the worst of the RFI, which simply sets the power of all RFI spikes above a running threshold to zero, and the subsequent analysis ignores them. An example of the raw and cleaned spectra is given in Fig. 11.

The squaring, summing, and cleaning process was repeated for both the off-Moon and on-Moon (center and limb) spectra for each antenna/polarization, and the off-Moon power-spectrum is subtracted from the corresponding on-moon spectra. Taking the square root gave the required $|b(\nu)|$ corresponding to the lunar contribution as required for Eq. (21). Note that we make the approximation $|b(\nu)| \simeq b(\nu)$ assuming that the dedispersion filter keeps the phase constant across the band. This was then divided by the product $\sqrt{Z_0 F_M(\nu)\Delta t}$ to give $|k(\nu)|$.

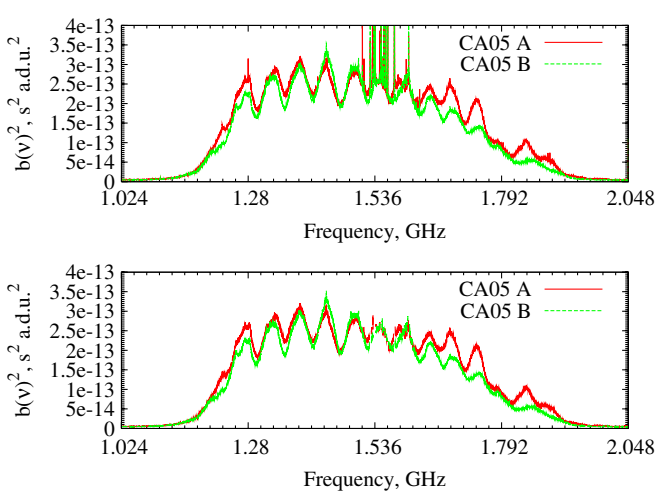

FIG. 11 (color online). Raw (top) and cleaned (bottom) spectra for the off-Moon pointing of May 18th on CA05.

D. Results of the calibration

1. Fitting for $k(\nu)$

In order to characterize $k(\nu)$ in a meaningful way, a piecewise linear approximation to $k(\nu)$ was performed. Figure 12 shows the fits for CA01 A in February 2008—four fits have been used, with different frequency ranges for each of the February and May periods. Also shown is the mean $\bar{k}(\nu)$, which has been fitted to the bandwidth 1.1–1.8 GHz in the case of February. For simulation purposes, the piecewise-linear fit to the bandwidth was used. Note that we have smoothed over the oscillations in $k(\nu)$, which are caused by interference between the dispersion-corrected signal from the filters, and a small reflection from the filter connection point—this reflection is also the cause of the prepulse observed in Fig. 5.

While some sensitivity is not included by limiting the range of the fitted bandwidth, including this range in the fit would artificially reduce $\bar{k}(\nu)$ at lower frequencies where a signal is more likely to be observed. Conversely, taking the fit below the low-frequency cutoff would have led to an overestimate of the sensitivity at low frequencies where the signal is stronger. Unsurprisingly, the ranges which gave a

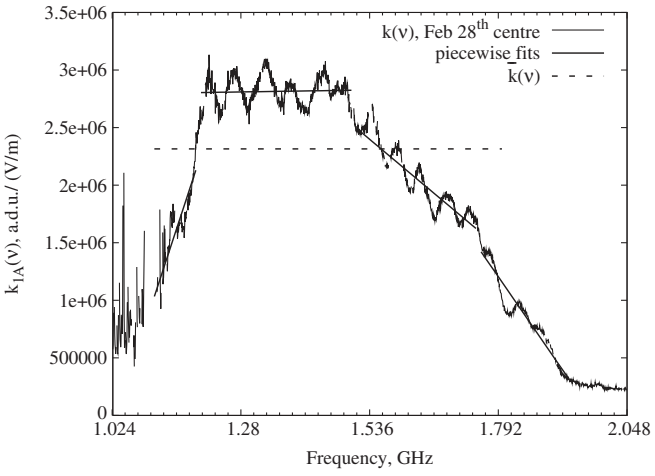

FIG. 12. $k(\nu)$ as measured for February 28th for CA01 A based on lunar center/off-Moon, piecewise fits to $k(\nu)$. Dashed line shows the mean $\bar{k}(\nu)$.

good trade-off between these effects and artificially reducing the effective bandwidth $\Delta\nu$ were close to the nominal bandwidth of 1.2–1.8 GHz.

Only one calibration was performed in February, and no cross-checking was possible. In May, it was found that while fits from both May 19th measures and the limb-off-Moon fit of May 18th were always in good agreement ($\pm$ 3%), the lunar center/off-Moon fits of May 18th were consistently low by 5–8%. Therefore these were excluded, and the fits averaged over the remaining data. For February, it may therefore be that a similarly low (or high) result was obtained. Such a systematic error is nonetheless small compared to other uncertainties in our sensitivity calculation, so we do not carry this error through our calculation.

2. Conversion to an effective V/m/MHz threshold

Using the piecewise-linear approximations to $\bar{k}(\nu)$ it is possible to calculate the thresholds in V/m/MHz given the thresholds in a.d.u. These were constantly altered throughout the experiment. The thresholds varied significantly between data channels and over time, since the thresholds were chosen to keep the trigger rate on each channel (rather than the thresholds themselves) constant.

Since a positive detection requires a threefold trigger, it is useful to define an effective signal detection threshold over all antennas. A good measure is to choose a mean V/m/MHz signal strength that over the bandwidth will have a 50% probability of triggering all three antennas. The random noise component can either increase or decrease the measured signal, so we require sufficient intrinsic signal strength above each individual antenna threshold that the chance of the random component pushing the signal below threshold is small. Thus the effective threshold is dependent upon this random component. The individual antenna thresholds were calculated from the mean recorded spectra from the relevant limb/center-pointing calibrations by averaging the RMS signal over the entire 1.024 GHz bandwidth, and converting the measured RMS signal in a.d.u. into V/m/MHz using $\bar{k}$. During times of significant out-of-band RFI, the effective thresholds will vary due to a greater RMS signal, but since these occasions are both rare and have a low effective efficiency, their contribution to the average threshold will be negligible and is neglected here.

Assuming a normally-distributed RMS field strength, the probability of the total of signal plus noise falling above threshold for any given signal strength can be readily calculated, and thus the probability that the global condition (`CA01A OR CA01B`) `AND` (`CA03A OR CA03B`) `AND` (`CA05A OR CA05B`) will be met. The detection probability is thus dependent on the alignment of the field vector with the A and B receivers—since the trigger condition is `A OR B`, the probability is highest when the field vector is parallel with either the A or B polarization directions, and lowest when it is 45° from both. Therefore the ''effective threshold'' is defined for a signal polarized at 22.5° (i.e. halfway between 0° and 45°) to either A or B. Since in general both the thresholds and RMS values are different for each polarization, we calculate the effective thresholds for signals polarized at both 22.5° (67.5°) and 67.5° (22.5°) to the A (B) receiver directions and average the results. By varying the raw signal strength until the calculated threefold detection probability was 50%, the effective thresholds could be calculated.

Doing so, we found that whereas each individual antenna trigger threshold was in the range 1.1–1.3 $\times$ 10^{-8} V/m/MHz, the effective thresholds for a global trigger were in the range 1.45–1.6 $\times$ 10^{-8} V/m/MHz, i.e. an increase in threshold (decrease in sensitivity) of approximately 25%. In comparison, adding all three antenna voltages coherently (gain of $\sqrt{3}$ in signal-to-noise) and detecting at a higher level of $V_{\mathrm{thresh}} = 9.5V_{\mathrm{RMS}}$ (so the probability of a false detection for a ~30-hr experiment would be less than 0.1%; there would no longer be a coincidence check) would have produced an effective threshold a few percentage *less* than the individual antenna thresholds, i.e. 1.05–1.25 V/m/MHz. Thus our inability to combine the signals coherently reduced our sensitivity by approximately 30%.

3. Comparison with a possible experiment at Parkes

An alternative instrument to the ATCA is the Parkes 64 m single-dish radio telescope, with an effective bandwidth of 300 MHz in the 1.2–1.5 GHz range. While the total sensitivity (here, area-bandwidth product) compared to the six ATCA antennas at 600 MHz bandwidth is 30% lower, with current technology we are unable to take advantage of the full ATCA collecting area, so we present a brief comparison of the two instruments. Approximate scaling from ATCA to Parkes would suggest that: (i) we gain a factor of ~9 in area compared with one 22 m dish; (ii) we loose a factor of ~2 because we do not have a triple coincidence trigger and so must set the trigger threshold higher; (iii) we loose a factor of ~2 because of the smaller bandwidth at Parkes; (iv) there is a modest gain because the lowest frequency is 1 GHz and not 1.2 GHz; (v) there is a modest gain because of the higher fraction of high quality RFI-free on-Moon time, though a lack of baseline may make RFI discrimination more difficult; (vi) there is a loss of a factor 2–3 because the Parkes multibeam receiver can cover less of the lunar limb. Factors (i)–(iv) reduce the neutrino energy threshold by $\sim\sqrt{9/(2\times 2)}$, i.e. overall the sensitivity for our ongoing experiment at Parkes should be more than twice as sensitive as our 2008 experiment using the ATCA, while factors (v)–(vi) decrease the effective area to high-energy events by 50%. For targeted observations of potential sources of UHE particles (see Ref. [31]), the Parkes telescope will be even more suitable, since for a targeted observation, only part of the lunar limb would need to be observed.

VII. RESULTS

A. Search for lunar pulses

The main search criteria used for eliminating false events were the timing requirements. The search window is given by the apparent angular width of the Moon in the East-West direction, since the North-South component is unresolved by the East-West baseline. This is $\sim 0.5°$ at transit (when the Moon achieves its greatest elevation), and considerably less near Moon-rise/set. This gives an intrinsic time-window of up to 23 ns (46 samples) over the maximum baseline of 765 m. While neither the raw nor the correlation-corrected times can be completely trusted, true lunar pulses will have a sharp time structure which will allow only a small variation in trigger times between antennas. Alternatively, those with extended structure (i.e. multipeaked electromagnetic showers viewed away from the Cherenkov angle) will be due to the highest energy showers and therefore strong enough to give a correct correlation.

Performing the search over both observation periods resulted in 60 candidates. Note that for any given lunar position there will always be two points on the horizon (one North and one South) which will have the same timing solution for an East-West baseline. Our search criterion is illustrated graphically in Fig. 10 (see Sec. V), where both the apparent direction of the Moon and the times and origins of candidate signals are plotted. Candidate origins plotted for May 17 do not appear to be consistent with the lunar position because we have allowed a larger time window in the search due to an uncertainty in the timing calibration for that night (as previously noted). Note that all candidate events were detected during periods of intense RFI.

The candidate events were then searched through by eye for pulselike events, and it was found that a majority of the candidates had a narrow-band RFI signature, with the recorded time-domain signals being strong over the entire buffer length. We did not use a more quantifiable measure than 'pulselike' simply because the narrow-band RFI was so obvious and strong when present, and some "pulses" had duration up to 30 ns. Since at these extremely high energies, multiple cascade signatures (e.g. from nearby hadronic and purely electromagnetic cascades) might

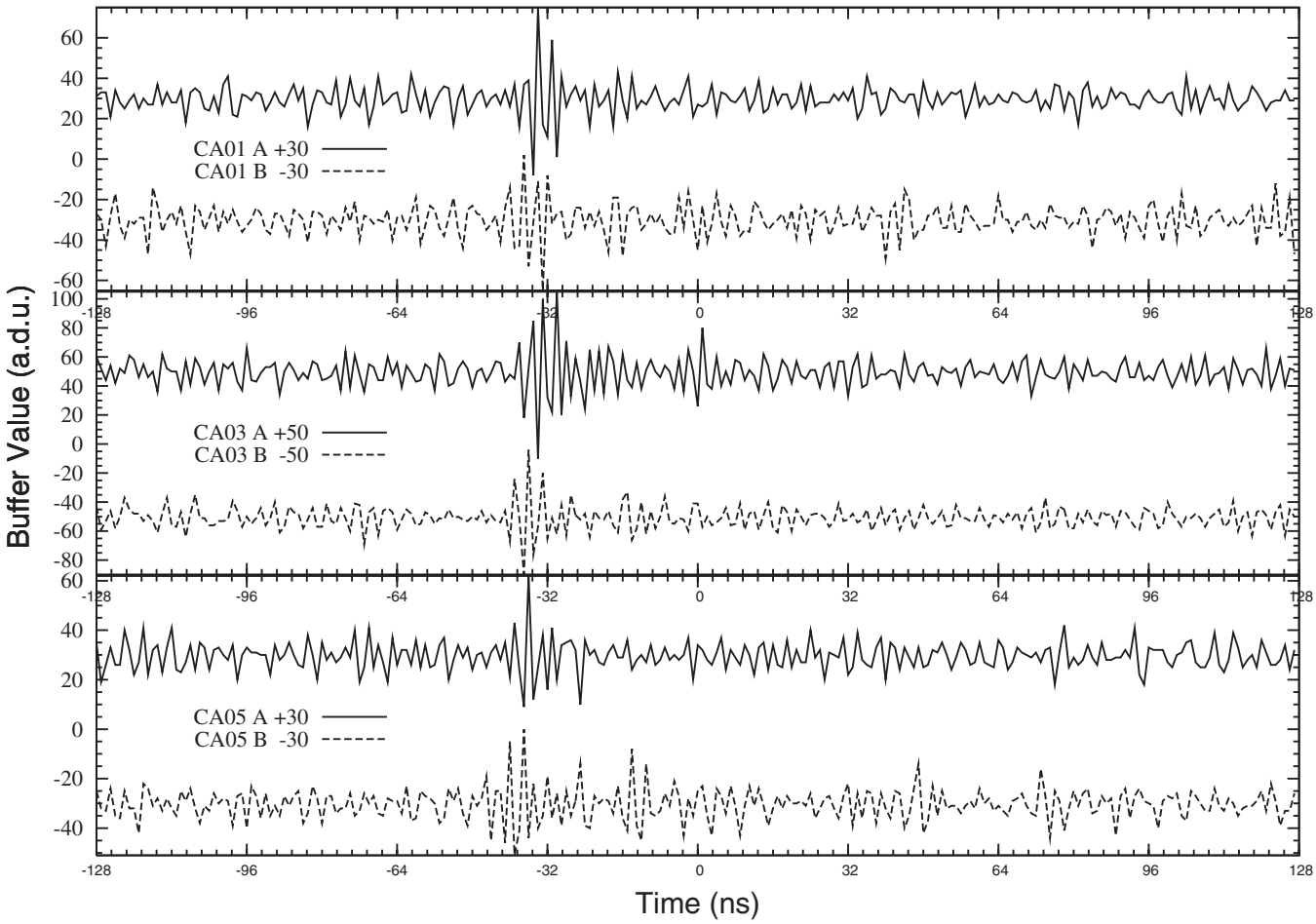

FIG. 13. A narrow time structure event from February 27th. Note that the signal has been displaced vertically by ± 30 as indicated for display purposes.

cause a lengthening of the expected pulse profile, we preferred to use timing criteria only if possible.

A minority of events—16 in total—had a narrow time-structure, an example of which is given in Fig. 13. All came within a two-hour period on February 27th, which was one of the most RFI-intense periods of all the observations. These could not be immediately excluded by eye, and had to pass more stringent tests. These are described below.

Ensuring possible origin to within sampling accuracy

The search algorithm allowed both small deviations from a far-field event, and small offsets in direction from the Moon, to account for potential errors in the automated alignment process. A check by eye of the corrected alignment times, if necessary including further adjustments, would be expected to yield accurate timing information in cases where the detected event has significant time-structure, as is the case with all 16 candidates. The correlation-corrected times occasionally needed further adjustment by one sample on a single baseline. For each candidate, the resulting alignment was compared visually to that required for the event to have a far-field origin; this was done quantitatively by comparing the buffer trigger times for CA03, t_3, to that expected (t_3') from t_5 and t_1:

$$t_3' = ((t_5 - t_1)(b_{13}/b_{15}) + t_1). \tag{23}$$

where b_{13} and b_{15} are baselines between antennas CA01 and CA03, and CA01, and, CA05, respectively. An example of this procedure is given in Fig. 14. In no case did any of these events appear to be a far-field event. In most cases, structure was evident in both polarizations, but was so weak in one that the other only could be used for determining the alignment—however, an alignment to within sampling accuracy could always be obtained. Since at these times the Moon made an angle of nearly 90° to the ATCA baseline, events within 360 km would result in a wave-front curvature with measurable differences between t_3 and t_3'—in the case shown in Fig. 14, the distance is of order 100 km and so this event can not have a lunar origin.

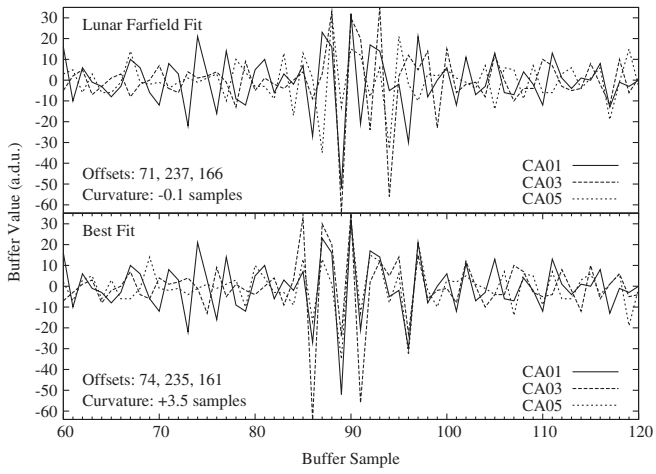

FIG. 14. Comparison of best far field-fitted alignment (top) with the best unrestricted fit (bottom) for polarization B on one of the 16 narrow-time-structure candidates on February 27th, for the values of the offsets (Δt_{31}, Δt_{51}, Δt_{53}) shown. The ''wave front curvature'' is given by subtracting the measured t_3 from the expected value t_3' given by Eq. (23).

In principle we could have also used the expected dispersion measure as a test to verify a pulse being of lunar or terrestrial origin. However, we deliberately chose observing times when the dispersion was low, and so this reduced the power of such a test. Since our timing criteria were already sufficient to exclude all candidate events as RFI we did not pursue this approach.

B. Effective apertures to an isotropic flux

The simulation program described by James and Protheroe [30] was modified to weight the frequency spectrum output over the bandwidth by $k(\nu)/\bar{k}$ using the piecewise linear approximation. The sensitivity of the experiment did not remain constant, but this was taken into account by running simulations using the lowest and highest values of $E_{\rm thresh}$ for each of the observation periods.

The deviation of the true TEC compared to that designed into our dedispersion filters changed our sensitivity continuously. The average peak recorded signal strength as a fraction of intrinsic peak strength (Fig. 8) for each of the observation periods was folded into the simulations for different combinations of the two extreme Cherenkov spectra and the lowest, average, and highest sensitivity.

It was found that changing the angles of the polarized receivers with respect to the lunar limb varied the calculated isotropic apertures to neutrinos above 10^{21} eV by less than 1%, and at most 4% at 10^{20} eV, where the apertures are in any case very small.

The two major uncertainties in this calculation are the UHE neutrino interaction cross-sections, and the effects of small-scale surface roughness (SSR), both of which are dealt with in detail in the appendices. In the following results, we do not incorporate the uncertainty in the cross-section for the simple reason that the uncertainty itself is so uncertain, since the scope for new physics at such high center-of-mass-energy collisions is large. Rather, we summarize the results of Appendix A by stating that a doubling (halving) of the cross-section results in an increase (decrease) in the effective aperture by a factor of approximately 1.88.

For the effects of small-scale surface roughness, we develop a toy model, and show both standard estimates (''ATCA no SSR'') and estimates adjusted for the results of calculations using this model (''ATCA SSR''). This model, while useful for understanding SSR phenomenology, is much less sophisticated than this topic requires, and the results based on it should be interpreted more as guides to indicate the nature of small-scale surface-roughness effects. The important result is that whereas traditionally

the effects of SSR were thought of as entirely negative, since the effect is to reduce the coherence of the wave front over the cascade length, the resulting increase in angular spreading of the radiation makes a detection at the highest energies more likely. Therefore, the calculations including SSR have a lower effective aperture at low neutrino energies, and a much higher aperture at the highest energies. Future work is expected to provide a more quantitative estimate of SSR effects.

Apertures and limits to an isotropic flux

The resulting range of effective apertures to an isotropic flux from each period is given in Fig. 15, assuming the presence of a radio-transparent megaregolith. Also plotted are the effective apertures from prior experiments as calculated by James and Protheroe [30]. For our ATCA observations, the threshold is lower than in past lunar Cherenkov experiments (since our high bandwidth has compensated for the smaller dishes), while the effective aperture at high energies is greater (due to increased coverage of the lunar limb and lower frequencies). Unlike the previous experiments with larger dishes, the sensitivity to UHE neutrinos is higher in the center-pointing mode (Feb 2008) than in the limb-pointing mode (May 2008), since the beam-width of ATCA near 1–2 GHz is comparable to

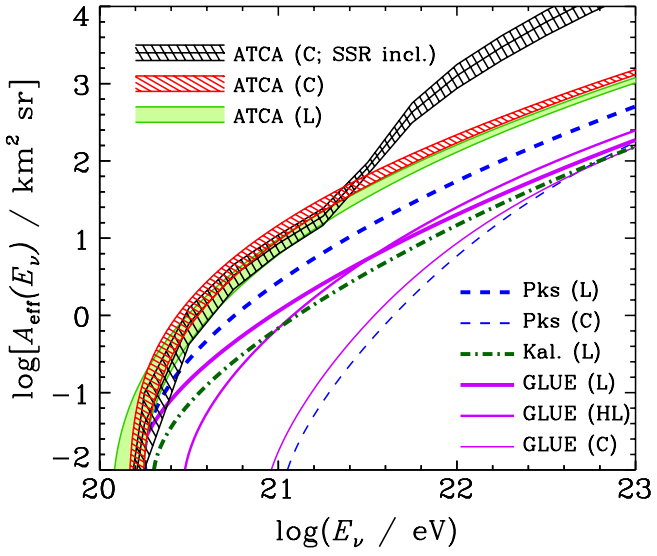

FIG. 15 (color online). The range of effective apertures (see text) for the LUNASKA February 2008 center-pointing (C) and May 2008 limb-pointing (L) ATCA observations, compared to that from previous experiments at Parkes (“Pks”), Kalyazin (‘Kal.’), and Goldstone (“GLUE”), in both limb- (“L”), half-limb- (“HL”), and center- (“C”) pointing modes (see [30]), assuming the existence of a subregolith layer of comparable dielectric properties to the regolith itself. We also show the effect on the aperture for the (center-pointing) Feb. 2008 observations including our adjusted toy model of small-scale surface roughness (C, SSR incl.) (see Appendix B), which is the reason for the abrupt (and artificial) change in aperture near 2×10^{21} eV.

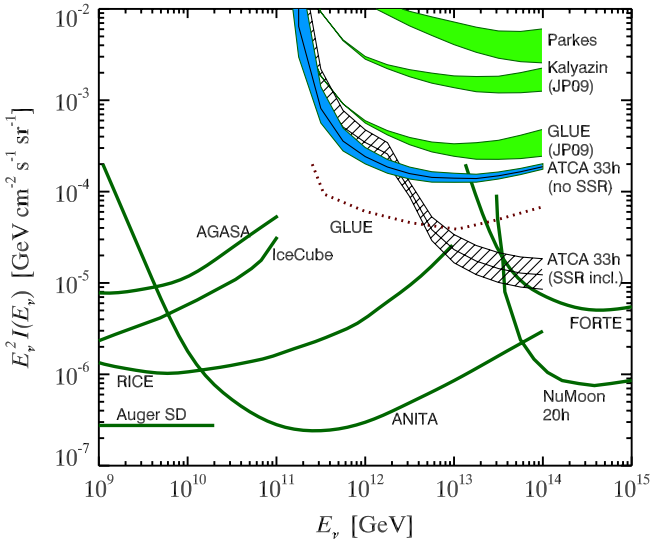

FIG. 16 (color online). Model-independent 90% confidence limits, i.e. $2.3/[t_{\rm eff}A_{\rm eff}(E_\nu)]$ for our nominal 33.5 hr observations (effective on-time $t_{\rm eff} = 26.15$ hr), on a total flux of UHE neutrinos (adjusted for all neutrino flavours) from our 2008 ATCA observations assuming a subregolith layer, both using the standard modeling (“ATCA no SSR”) and using our adjusted toy model of small-scale surface roughness (“ATCA SSR incl.”). In the “SSR” case, the abrupt transition near 2×10^{12} GeV is a model artefact (see Appendix B). Also, from previous experiments: GLUE [11]; IceCube [55]; RICE [48]; ANITA [49]; FORTE [43]; NuMoon [24]; revised estimates by James and Protheroe [30] for Parkes, GLUE, and Kalyazin are shown by hatched bands (upper boundary—limit for 10 m regolith; lower boundary—10 m regolith plus 2 km subregolith); Auger surface detectors [56]. The range on the band labeled ATCA reflects experimental uncertainties, while for previous experiments (where applicable) reflects the inclusion or otherwise of a subregolith layer.

the apparent diameter of the Moon. Note also that previous calculations (Refs. [25,28,45]) have not included the loss from a noninfinite sampling rate, and so their effective aperture should be reduced somewhat.

The limit on an isotropic flux of neutrinos arising from our combined 2008 observations to a UHE ν flux is given in Fig. 16 as the band labeled “ATCA no SSR”. Also shown is the limit—“ATCA SSR”—when our toy model of small-scale surface roughness (see Appendix B) is included, and the limits from previous experiments, including GLUE [11] (dashed line labeled “GLUE”) which is now believed to be approximately an order-of-magnitude too low as pointed out by James and Protheroe [30] and confirmed by Gayley *et al.* [29]. The GLUE limit as revised upward by James and Protheroe is shown by the band line labeled “GLUE (JP09)”.

VIII. SUMMARY AND CONCLUSION

In 2008 we carried out observations of the Moon at the Australia Telescope Compact Array using the lunar

Cherenkov technique to search for the signatures of UHE neutrinos. Although no lunar pulses of any source were positively identified, the instantaneous apertures for all the observations were the most sensitive yet achieved using the technique. The corresponding limits on an isotropic flux are not as strong as those from RICE and ANITA, but our methods to improve sensitivity to certain patches of the sky—which, along with our limit on the UHE neutrino flux from Centaurus A and the Galactic Center [34], will be published separately—were a success: we found the exposure from our observations to Centaurus A to be higher than all previous experiments at neutrino energies of 10^{22}–10^{23} eV and above.

The lack of detection of nanosecond lunar pulses reported here is consistent with limits set by the ANITA experiment. Importantly, our methods to discriminate between true lunar pulses and RFI were very successful: we can be extremely confidant that no true lunar Cherenkov pulses were detected simultaneously by all three antennas, despite having of order 10×10^6 trigger events. This demonstrates primarily the power of nanosecond timing over a significant baseline, which was made possible by our use of a very wide (here, 600 MHz) bandwidth, and was the main criterion used to discriminate against false events. Importantly, it was found in Sec. that for events of reasonable time-structure (the category into which all candidates must fall), the automatic procedures produced times accurate to better than 1 ns. Therefore, relying on such a procedure to search for candidate pulses in the future is justified, making a comparable analysis for a long observation run of a month or more feasible.

Our first estimates of the effects of small-scale surface roughness on the detectability of lunar Cherenkov pulses at high frequencies—and the potential 2 orders of magnitude improvement in the effective aperture at the highest energies, and order-of-magnitude worsening of the threshold—only serves to emphasize the importance of further work. Since these effects are indicative of ''messy'' signals caused by roughness-induced interference along the length of the cascade, it also suggests that timing criteria on signal origin (i.e. that the signal comes from the Moon) be used instead of criteria on the pulse shape (i.e. that it is very close to impulsive). Our use of such criteria to eliminate all our candidate events proves that this is possible. It is important to note that the energy range at which small-scale surface-roughness effects are expected to increase the strength of our limit is the range at which our ATCA experiment is most competitive.

For our observations, the use of an analog dedispersion filter proved highly successful. The dispersion measure assumed in the filters' construction turned out to be very close to the actual values during observation periods, so that incorrect dedispersion lost us less sensitivity than triggering inefficiency due to our noninfinite sampling rate. Though such filters must inevitably be superseded by a digital method, their continued use in the meantime will be valuable. Conversely, the finding that the loss from a finite sampling rate was greater for our simple trigger algorithm than that from incorrect dedispersion is extremely important, and that in fact our ''over''-sampling was an important factor in increasing (or rather, reducing the loss of) sensitivity. In future observations therefore the use of a smarter trigger algorithm that uses the already fully available information to reconstruct intermediate trigger values should be used, and perhaps should take as high a priority as digital dedispersion.

Compared with an alternative single-dish experiment at Parkes, our experiment at the ATCA provided more effective area to high neutrino energies at the expense of less sensitivity to lower energy events. Since the parameter space at which the ATCA experiment is superior is best explored by low-frequency experiments such as NuMoon, we have transferred our efforts to utilizing the Parkes dish, the results of which will be reported in a future contribution. We point out, however, that multitelescope systems (such as the SKA and its pathfinders) will be more sensitive than single-dish experiments, and that our ATCA experiments would have been significantly more sensitive had we not been limited to using only three antennas due to telescope upgrade delays.

For future experiments at the ATCA or at other radio telescope arrays, further improvements such as real-time coincidence logic between three or more antennas, or even the ultimate goal of a coherent addition of the signals, would also improve the sensitivity. Without a further analysis of the typical RFI structure, it is not possible to determine the utility of real-time anti-RFI logic, though given the prevalence of RFI-triggered pulses, this too should be considered.

The lessons learned above should in all cases be applicable to any use of the lunar Cherenkov technique with an array of radio antennas. The advantage of using a giant radio array such as the SKA to search for lunar pulses has only been highlighted by these observations, especially since it will be placed in a low-RFI environment.

We have demonstrated techniques being developed by us ultimately for use with the Square Kilometer Array, and have been able with only 6 nights of observations using the ATCA to produce the lowest limit to an isotropic UHE neutrino flux below 3×10^{22} eV of any lunar Cherenkov experiment. While at present the isotropic limits from lunar Cherenkov experiments are not competitive with RICE [48], ANITA [49] and (above 3×10^{22} eV) NuMoon, use of the SKA in several years' time for lunar Cherenkov observations will provide a very powerful technique for UHE neutrino astronomy [30]. With an estimated sensitivity to neutrinos 100 times less energetic than those detectable with our experiment at the ATCA, the SKA will be able to probe the as-yet untested predictions for a flux of neutrinos from the GZK process. Furthermore, our current

experiment has been able to access regions of the sky not accessible to ANITA and NuMoon, and with better exposure than RICE above 3×10^{22} eV. Our flux limits to UHE neutrinos from Centaurus A will be discussed in a future paper.

ACKNOWLEDGMENTS

The Australia Telescope Compact Array is part of the Australia Telescope which is funded by the Commonwealth of Australia for operation as a National Facility managed by CSIRO. This research was supported by the Australian Research Council's Discovery Project funding scheme (project numbers DP0559991 and DP0881006). J. A-M. thanks Xunta de Galicia (PGIDIT 06 PXIB 206184 P. R.) and Consellería de Educación (Grupos de Referencia Competitivos—Consolider Xunta de Galicia 2006/51).

APPENDIX A: VARIATION OF APERTURE WITH NEUTRINO CROSS-SECTION

The greatest unknown in the calculation of the aperture is that of the UHE neutrino-nucleon cross-section $\sigma_{\nu N}$, since this requires the extrapolation of experimental data over many orders of magnitude—hence the finding of Gandhi *et al.* [50] that the cross-section could vary by a factor of $2^{\pm 1}$ at 10^{20} eV [50]. This conclusion was born out after a more recent calculation by Cooper-Sarkar and Sarkar [51] using updated data from HERA estimated a neutrino-nucleon charged-current (CC) cross section which is approximately 30% lower at 10^{20} eV, and getting relatively smaller with increasing energy. There is also scope for ''new physics'' to alter the cross section even further.

Given the range of uncertainty even within ''standard physics'', the determination of the UHE neutrino-nucleon cross section is necessarily a scientific goal of UHE neutrino-detection experiments which is inseparable from the measurement of the UHE neutrino flux itself, and in this context, instead of limits on the flux having a cross-sectional uncertainty, the limits should be set in flux–cross-section space. However, due both to convention and the complexity of doing so, they are not. Instead, to estimate the effect of uncertainty in the cross-section on our calculated effective area and flux limits, we calculate the fractional rate of change in the effective aperture $A_{\rm eff}$ with the fractional rate of change in cross section, i.e. $\frac{\sigma_{\nu N}}{A_{\rm eff}} \frac{dA_{\rm eff}}{d\sigma_{\nu N}}$. In the limit where neutrinos cannot penetrate a large part of the Moon and are seen only when they interact almost immediately in a thin layer at the Moon's surface ('down-going' interactions), we expect $\frac{\sigma_{\nu N}}{A_{\rm eff}} \frac{dA_{\rm eff}}{d\sigma_{\nu N}} = 1$, i.e. doubling the cross-section doubles the interaction rate, and vice-versa (a similar effect is reached if the entire Moon is transparent to neutrinos, but this is far from reality). Since this limit is approached for high neutrino energies observed at high frequencies, we expect results to be close to 1. Any contribution from 'upcoming' neutrinos (neutrinos having penetrated a significant part of the Moon before reaching the surface) would reduce the result below 1, while no mechanism exists to increase the result above 1.

TABLE VI. The effects of changing cross section on the simulated effective aperture, assuming the neutral-current cross-section scales with the charged-current cross section for the calculation of Cooper-Sarkar and Sarkar [51].

E_ν	10^{21} eV	10^{22} eV	10^{23} eV
$\frac{\sigma_{\nu N}}{A_{\rm eff}} \frac{dA_{\rm eff}}{d\sigma_{\nu N}}$	0.9	0.915	0.93
$\sigma^{\rm CSS}_{\nu{\rm NCC}}/\sigma^{\rm GQRS}_{\nu{\rm NCC}}$	0.55	0.42	0.30
$A^{\rm CSS}_{\rm eff}/A^{\rm GQRS}_{\rm eff}$	0.60	0.46	0.35

To determine the sensitivity to the cross section, we varied the cross section by $\pm 20\%$, and ran simulations for three primary neutrino energies—10^{21}, 10^{22}, and 10^{23} eV—using the full range of ATCA sensitivities (best- and worst-cases) and configurations (February and May observations). We found the effect of varying the cross section at a given energy was the same for all cases, and that over this range of σ, $\frac{\sigma_{\nu N}}{A_{\rm eff}} \frac{dA_{\rm eff}}{d\sigma_{\nu N}}$ was also constant at a given energy. Thus in Table VI we give one value only of $\frac{\sigma_{\nu N}}{A_{\rm eff}} \frac{dA_{\rm eff}}{d\sigma_{\nu N}}$ for each primary neutrino energy, averaged over all cross sections and observer configurations. That the values are very close to one confirms that down-going neutrinos dominate the detected interactions, especially at high energies, so that a reduced (increased) estimate for the neutrino-nucleon cross-section would proportionately decrease (increase) the ATCA experimental aperture, with a corresponding increase (decrease) in the flux limit set from this experiment. Whether the cross section can be deconvolved from the flux using (for instance) the average origin of the signal is a subject for a future contribution. We also give in Table VI the reduced values of the charged-current neutrino-nucleon cross-section $\sigma_{\nu{\rm NCC}}$ using the fit given in Eq. 3.5 of Cooper-Sarkar and Sarkar (CSS) and Gandhi *et al.* (GQRS), together with the implied reduction in effective area $A^{\rm CSS}_{\rm eff}/A^{\rm GQRS}_{\rm eff}$ under the assumption that the neutral-current cross-section scales with the charged-current cross section in the CSS calculation.

APPENDIX B: VARIATION OF APERTURE WITH ROUGHNESS MODEL

Current models of lunar surface roughness use a single surface slope over the entire length of the cascade through which radiation refracts. This is only an approximate treatment, as discussed by James and Protheroe [30], since it takes the typical deviation at scales of order a wavelength, and treats it as a large-scale (greater than a cascade length) phenomena. Here we define small-scale roughness to be that on a scale between a cascade length (typically a few

metres for hadronic cascades) and the wavelength in the medium. The consequences of restricting scales to this range is discussed later. The effect of small-scale roughness is to reduce the coherence between radiation from different parts of the cascade. This in turn broadens the angular width over which the radiation is emitted while reducing the peak strength, and also allows transmission for angles of incidence greater than the critical angle, which is an effect observed for rough optical surfaces [52].

We carry out simulations using a toy model for an extreme case in which radiation from different parts of a shower in a near-surface cascade will see different surfaces and thus be refracted semi-independently. We refer to the resulting effective aperture including our small-scale surface roughness model as $A^R_{\rm eff}$, while the effective aperture for the ''standard case'' without small-scale surface roughness is $A^S_{\rm eff}$. Because of interference effects, the true effective aperture is likely to be between these two extremes, and it may be reasonable to approximate this over a restricted frequency range by an ''adjusted'' effective aperture $A^A_{\rm eff} = rA^S_{\rm eff} + (1 - r)A^R_{\rm eff}$. First we describe the toy model, then the simulation method and the resulting aperture $A^R_{\rm eff}$. Interference effects and a method of determining r and hence $A^A_{\rm eff}$ are dealt with, and finally we discuss the validity of the approximations made and the necessity of a rigorous treatment of the effect of small-scale roughness.

1. Toy model calculations and results

Assuming the smallest roughness scale to which radiation is sensitive is that of a wavelength, a cascade of length L might see up to N_S ($\approx L_S/\lambda$) refractive surface elements, where L_S is the cascade length. Though it is unclear whether the applicable wavelength λ is that of the low-index or high-index medium, since our goal is to put an inclusive bound on the effects of such roughness, we choose $\lambda = \lambda_n$, where λ_n is the wavelength in the medium of highest refractive index. We also choose λ corresponding to the frequency $\bar{f} = (f_{\rm min} \times f_{\rm max})^{0.5}$. For our experiment at ATCA, $\bar{f} = 1.47$ GHz, so $\lambda_n = 11.8$ cm in the regolith ($n = 1.73$).

We calculate N_S by scaling the energy- and medium-dependent L_S from its value of $12\chi_0/\rho$ (12 radiation lengths given the medium density: ~4.7 m) for hadronic cascades in ice at 10 EeV [53] by 7.5% per decade in energy as per Williams [45]. Since in our treatment, each portion of the cascade would ''see'' a different refractive element, we break the cascade into N_S separate segments, rounding N_S up to take an integer value. Thus we arrive at a shower length given by Eq. (B1), and the number of shower segments N_S given by Eq. (B2):

$$L_S = 12(X_0/\rho)\left[1 + 0.075\log_{10}\left(\frac{E_S}{10\ \text{EeV}}\right)\right] \tag{B1}$$

$$N_S = L_S\left(\frac{n\bar{f}}{c}\right). \tag{B2}$$

We assume that each of the N_S segments contains an equal portion of the total excess tracklength of each cascade, so that the peak electric field amplitude from each is $1/N_S$ that of the cascade as a whole. We also assume that the segment has length L_S/N_S, so the width of the Cherenkov cone is correspondingly broadened by the same factor N_S. Table VII summarizes the scaling relationships and number of shower segments for hadronic cascades at energies of 10^{21}, 10^{22}, and 10^{23} eV in the regolith and megaregolith.

The radiation from each cascade segment is treated independently, with the simulated experiment able to detect none, all, or some of the cascade segments, with the detection probability of the primary neutrino being equal to one minus the probability that none of the individual cascade segments are detected. We calculate the transmission coefficients separately for each piece of surface, which results in the observed signal appearing to come mostly from those parts of the surface pointing roughly towards the observer. This method is identical to that described by James and Protheroe [30] for handling cascades from interactions of secondary μ, τ, and ν. However, it ignores the possibility of interference between the radiation from cascade segments, an effect which is unimportant for secondary interactions separated by large distances. We make an approximate adjustment for such interference by calculating an ''adjusted'' effective aperture $A^A_{\rm eff}$ in Sec. B 2—suffice to say for now that $A^A_{\rm eff}$ must lie between $A^S_{\rm eff}$ and $A^R_{\rm eff}$.

To generate a surface roughness deviate, we first generate a deviate on the length scale L_S of the entire cascade as per James and Protheroe [30], where the slope tangents in each direction are sampled from a normal distribution with mean 0 and standard deviation $\tan S_{\rm rms}$ given according to Eq. (B3) (modified from Olhoeft and Strangway [54] by substituting $L_S/1$ m for $\lambda/1$ cm):

$$\tan S_{\rm rms} = 0.105 L_S^{-0.22}. \tag{B3}$$

TABLE VII. Parameters relating to the number of subshowers in the surface-roughness estimate, and some typical parameter values. Energies relate to the total hadronic cascade energy, which is typically 20% that of the primary neutrino energy.

Layer	X_0 (g/cm^2)	ρ (g/cm^3)	X_0/ρ (cm)	L_S (m) 10^{21} eV	10^{22} eV	10^{23} eV	$\lambda_{\bar{f}}/n$ (m)	N_s 10^{21} eV	10^{22} eV	10^{23} eV
Regolith	22.59	1.8	12.55	1.51	1.62	1.73	0.118	13	14	15
Megaregolith	22.59	3.0	7.53	0.895	0.962	1.03	0.082	11	12	13

The distribution of surface roughness experienced by radiation at wavelength λ_n (m) is found be replacing L_S by λ_n in the above equation. The extra roughness at small length scales can be thought of as additional small-scale deviation $\Delta \tan S_{\rm rms}$ superimposed over the large-scale roughness, which must produce the correct total value of $S_{\rm rms}(\lambda_n)$. Since the small-scale deviation in this model is independent of the large-scale deviation, we find:

$$\tan^2 S_{\rm rms}(\lambda_n) = \tan^2 S_{\rm rms}(L_S) + (\Delta \tan S_{\rm rms})^2 \qquad \text{(B4)}$$

Substituting the formula for $\tan S_{\rm rms}$ from Eq. (B3) into Eq. (B4) then gives the value of the additional surface deviate:

$$\Delta \tan S_{\rm rms} = 0.105(\lambda_n^{-0.44} - L_S^{-0.44})^{0.5}. \qquad \text{(B5)}$$

This gives a typical value for $\Delta \tan S_{\rm rms}$ of 8°; we approximate $\Delta \tan S$ for each individual subshowers to be independent of each other for simplicity. Thus, for each cascade, we first calculate the length and generate a bulk surface normal by randomly sampling two slope tangents according to Eq. (B3), then for each subshower we modify the bulk surface normal by adding extra surface tangents sampled according to Eq. (B5).

The additional complexity caused by breaking the cascade into segments means that we model only a simplified version of our experiment, using three antennas with a flat bandpass and single, circularly-polarized receivers operating in coincidence, with thresholds only approximately that of our real experiment. We run the simulation both with (treatment described above) and without (standard treatment) small-scale surface roughness for primary neutrino energies in the range $10^{20} < E_\nu < 10^{23}$ eV. Though the absolute values of the effective apertures $A^S_{\rm eff}$ and $A^R_{\rm eff}$ have little meaning for this fictional experiment, they are still illustrative to plot, which we do in Fig. 17.

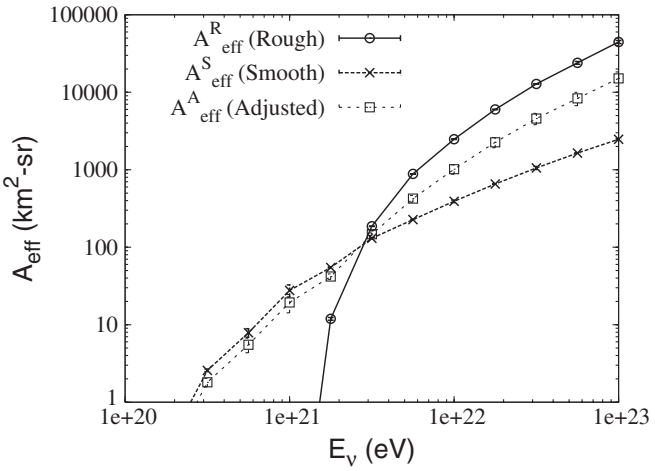

FIG. 17. Effective apertures of a fictitious experiment, calculated using large-scale roughness only ($A^S_{\rm eff}$), our small-scale roughness approximation ($A^R_{\rm eff}$), and an adjusted aperture which is a linear combination of them both ($A^A_{\rm eff}$—see Sec. B 2).

Comparing $A^S_{\rm eff}$ with $A^R_{\rm eff}$, the effect of small-scale roughness is significant. Since the peak emission from each cascade segment is a factor of N_S (~ 10) lower than that of the whole cascade, the effective neutrino energy detection threshold has been increased by a factor of the same order. However, at the highest energies ($\gtrsim 10^{22}$ eV), the probability of detection has increased by a factor of order 100, since the emission from each cascade is broader, and there are more cascades. In all, the effect of small-scale roughness on the detection probability mimics that of observing at a lower frequency in the case when no such roughness is considered, though the expected time-domain signature would be quite different.

2. Estimate of interference effects

The aperture $A^R_{\rm eff}$ calculated by modeling small-scale surface roughness, as previously noted, excludes interference between different cascade segments. Unlike radiation from two separate cascades, which if exiting the Moon in the same direction would be seen as two independent signals by a detector, the arrival times of radiation from two cascade segments will likely be separated by less than their duration—that is, they interfere. At one extreme (''case 1''), all the cascade segments will see the same surface and their radiation will exit in the same direction. Thus they interfere according to the standard Cherenkov condition, and the standard modeling producing $A^S_{\rm eff}$ is the correct treatment. At another extreme (''case 2''), the refracted radiation patterns from each cascade segment will not overlap, the cascades can be treated independently, and the results generated from our small-scale roughness model (i.e. $A^R_{\rm eff}$) will be correct insofar as the surface generated is appropriate.

We model our results as a linear combination of these two extremes by comparing the calculated aperture $A^S_{\rm eff}(E_\nu)$ to that of $A^R_{\rm eff}(N_S E_\nu)$. On average, the peak strength of the emission of each cascade in the $A^S_{\rm eff}(E_\nu)$ calculation will be the same as that of each cascade segment in the $A^R_{\rm eff}(N_S E_\nu)$ calculation, while the width of the radiation patterns from the segments under rough modeling will be $k_L N_S$ times greater, where k_L allows for the slow growth of cascade length with energy:

$$k_L = (1 + 0.075 \log_{10} N_S)^{-1}. \qquad \text{(B6)}$$

Assuming no interference, the aperture in the rough 'R' case will be one factor of N_S times larger than the standard 'S' case due to there being N_S as many subcascades, and a further factor of $k_L N_S$ due to the increased width as described above. Thus we expect that the ratio $A^R_{\rm eff}(N_S E_\nu)/A^S_{\rm eff}(E_\nu)$ should be $k_L N_S^2 \sigma_H(N_S E_\nu)/\sigma_H(E_\nu)$, where σ_H is the cross-section for interactions producing hadronic cascades. This assumes that the interaction rate is

proportional to the cross-section, which is accurate to order 10% (see Appendix A). We also assume that all hadronic interactions are dominated by neutrino-nucleon interactions (also an order 10% approximation [30]), so that $\sigma_H \propto E^{0.363}$ [50], and thus:

$$A^R_{\rm eff}(N_S E_\nu)/A^S_{\rm eff}(E_\nu) = k_L N_S^{2.363}. \tag{B7}$$

If the interference is complete (radiation always exits in an identical direction), and we assume a detection probability of 1 within some part of the Cherenkov cone and 0 otherwise so that there is no gain in detection probability from seeing the emission from two cascade segments, then only one of the N_S cascades will be detected in the $A^R_{\rm eff}(N_S E_\nu)$ simulation, and we should find the ratio:

$$A^R_{\rm eff}(N_S E_\nu)/A^S_{\rm eff}(E_\nu) = k_L N_S^{1.363}. \tag{B8}$$

We thus define the fractional overlap r such that $r = 0$ indicates no interference ($A^R_{\rm eff}$ applies), and $r = 1$ complete interference ($A^S_{\rm eff}$ applies), i.e.:

$$A^R_{\rm eff}(N_S E_\nu)/A^S_{\rm eff}(E_\nu) = (1 - r)k_L N_S^{2.363} + r k_L N_S^{1.363}. \tag{B9}$$

Using $N_S = 13 \pm 1$, we plot $A^R_{\rm eff}(N_S E_\nu)/A^S_{\rm eff}(E_\nu)$ in Fig. 18, and fit for r to the high-energy regime where r is constant. Note that in this model the number N_s of surface pieces refers to the number upon which the radiation is incident, not the number an observer sees. We expect an increasing ratio at low energies where a larger fraction of the emitted radiation is partially detectable (detection probability being neither 0 nor 1), since then there is a gain in calculated aperture from two cascade segments radiating in the same direction. Though an increasing value of r is not observed at low energies—likely the effect is obscured by the large uncertainties—we nonetheless use only the range $E \geq 10^{21}$ eV for the fit, finding $r = 0.70 \pm 0.06$.

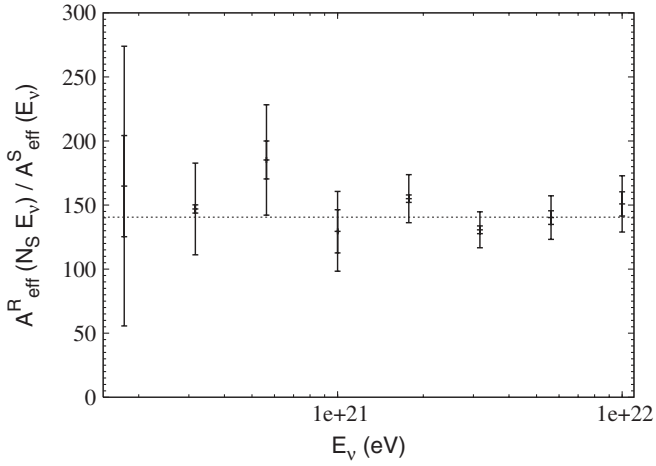

FIG. 18. The ratio $A^R_{\rm eff}(N_S E_\nu)/A^S_{\rm eff}(E_\nu)$. The error bars reflect both uncertainties in the apertures themselves from the Monte Carlo simulation (inner error bars), and also including the error from $N_S = 13 \pm 1$. The fit is to the range $E_\nu \geq 10^{21}$ eV only.

An adjusted aperture $A^A_{\rm eff}$ can then be calculated by $A^A_{\rm eff}(E_\nu) = rA^S_{\rm eff}(E_\nu) + (1 - r)A^R_{\rm eff}(E_\nu)$. This has added to Fig. 17 for our fictitious experiment. By assuming similar behavior for our real experiment with the ATCA, we can calculate an adjusted aperture from our standard aperture only:

$$A^A_{\rm eff}(E_\nu) = 0.7A^S_{\rm eff}(E_\nu) + 0.3k_L N_S^{2.363} A^S_{\rm eff}(E_\nu/N_S). \tag{B10}$$

The result has already been given for both our experimental aperture and limit in Figs. 15 and 16 respectively, by using the aforementioned values of r and N_S.

3. Assessment of accuracy

The model for small-scale surface roughness presented here is intended as a toy model which deals only with the most significant possible effects of small-scale roughness at high frequencies. For instance, the sudden change in slope around 2×10^{21} eV in Fig. 17 is purely an artefact of our superposition of two extreme models—there is no reason to expect that a rigorous calculation would produce any energy-dependent results sharper than the slow (logarithmic) increase in cascade length with particle energy.

In cases where the surface slopes are positively correlated, and/or when a cascade is sufficiently deep that the far-field conditions are satisfied at the surface over most of the cascade, then our model of treating the radiation from each cascade/surface piece independently breaks down. While our introduction of the overlap parameter 'r' goes some way to correcting for such correlation, in these cases the value of 'r' would likely be larger, so the effects of small-scale roughness estimated by our toy model are more likely to be overestimates than underestimates.

Our model also ignores roughness on scales smaller than a wavelength, which can not be dealt with by splitting the cascade into segments as in our toy model (it is not possible to produce multiple-refraction effects for structures of size less than that of a wavelength). However, we do expect such roughness to broaden the emission at the expense of peak refracted field strength—for our current model, this would mostly cause an increase in the overlap ratio r in our results. Therefore, we ignore subwavelength roughness until a more complete model can be constructed, which we leave to a future work. An additional approximation is that we have assumed only a single frequency for our

surface-roughness estimates, rather than a continuous range.

Despite these shortcoming, we have developed the first treatment of roughness on scales smaller than a cascade length, an important effect for high-frequency observations that has been ignored in all previous calculations. Whether this effect helps or hinders neutrino detection will depend upon the shape of the UHE neutrino spectrum. What we can say is that the difference in detection probability between high- and low-frequency observations may not be as dramatic as previously thought, but that a reconstruction of cascade parameters from a detected event may prove more difficult.

[1] J. Abraham *et al.* (The Pierre Auger Collaboration), Science **318**, 938 (2007).
[2] K. Greisen, Phys. Rev. Lett. **16**, 748 (1966).
[3] G. T. Zatsepin and V. A. Kuzmin, JETP Lett. **4**, 78 (1966).
[4] M. Takeda *et al.*, Astropart. Phys. **19**, 447 (2003).
[5] D. J. Bird *et al.*, Astrophys. J. **441**, 144 (1995).
[6] B. M. Connolly, S. Y. BenZvi, C. B. Finley, A. C. O'Neill, and S. Westerhoff, Phys. Rev. D **74**, 043001 (2006).
[7] J. Abraham *et al.* (The Pierre Auger Collaboration), Phys. Rev. Lett. **101**, 061101 (2008).
[8] R. U. Abbasi *et al.*, Phys. Rev. Lett. **100**, 101101 (2008); R. U. Abbasi *et al.*, Astropart. Phys. **32**, 53 (2009).
[9] T. Abu-Zayyad *et al.*, Astropart. Phys. **23**, 157 (2005).
[10] R. J. Protheroe, Astropart. Phys. **21**, 415 (2004).
[11] P. W. Gorham *et al.*, Phys. Rev. Lett. **93**, 041101 (2004).
[12] S. W. Barwick *et al.*, Phys. Rev. Lett. **96**, 171101 (2006).
[13] R. J. Protheroe and R. W. Clay, Pub. Astron. Soc. Aust. **21**, 1 (2004).
[14] H. Falcke, P. Gorham, and R. J. Protheroe, New Astron. Rev. **48**, 1487 (2004).
[15] G. A. Askaryan, Sov. Phys. JETP **14**, 441 (1962); **48**, 988 (1965).
[16] D. Saltzberg *et al.*, Phys. Rev. Lett. **86**, 2802 (2001).
[17] P. W. Gorham *et al.*, Phys. Rev. D **72**, 023002 (2005).
[18] P. W. Gorham *et al.*, Phys. Rev. Lett. **99**, 171101 (2007).
[19] J. Álvarez-Muñiz, E. Marqués, R. A. Vázquez, and E. Zas, Phys. Rev. D **68**, 043001 (2003).
[20] R. D. Dagkesamanskij and I. M. Zheleznykh, JETP Lett. **50**, 233 (1989).
[21] T. H. Hankins, R. D. Ekers, and J. D. O'Sullivan, Mon. Not. R. Astron. Soc. **283**, 1027 (1996).
[22] C. W. James, R. M. Crocker, R. D. Ekers, T. H. Hankins, J. D. O'Sullivan, and R. J. Protheroe, Mon. Not. R. Astron. Soc. **379**, 1037 (2007).
[23] A. R. Beresnyak, R. D. Dagkesamanskij, I. M. Zheleznykh, A. V. Kovalenko, and V. V. Oreshko, Astronomy Reports **49**, 127 (2005).
[24] O. Scholten *et al.*, Nucl. Instrum. Methods Phys. Res., Sect. A **604**, S102 (2009).
[25] O. Scholten *et al.*, Astropart. Phys. **26**, 219 (2006).
[26] E. Zas, F. Halzen, and T. Stanev, Phys. Rev. D **45**, 362 (1992).
[27] P. W. Gorham, K. M. Liewer, C. J. Naudet., D. P. Saltzberg, and D. Williams, in *Radio Detection of High Energy Particles—RADHEP 2000*, edited by D. Saltzberg and P. W. Gorham, AIP Conf. Proc. 579, 177 (AIP, New York, 2001).
[28] A. R. Beresnyak, arXiv:astro-ph/0310295v2.
[29] K. G. Gayley, R. L. Mutel, and T. R. Jaeger, Astrophys. J. **706**, 1556 (2009).
[30] C. W. James and R. J. Protheroe, Astropart. Phys. **30**, 318 (2009).
[31] C. W. James and R. J. Protheroe, Astropart. Phys. **31**, 392 (2009).
[32] S. Johnston *et al.*, Exp. Astron. **22**, 151 (2008); Pub. Astron. Soc. Aust. **24**, 174 (2007); www.atnf.csiro.au/projects/askap/.
[33] Special issue on The Australia Telescope [J. Electr. Electron. Eng., Aust. **12**, 103 (1992)]; Australia Telescope National Facility: http://www.atnf.csiro.au/ and pp. contained therein.
[34] C. W. James, R. J. Protheroe, R. D. Ekers, J. Álvarez-Muñiz, R. A. McFadden, C. J. Phillips, P. Roberts, and J. D. Bray, arXiv:0906.3766.
[35] R. D. Ekers, C. W. James, R. J. Protheroe, and R. A. McFadden, Nucl. Instrum. Methods Phys. Res., Sect. A **604**, S106 (2009).
[36] C. W. James, Ph.D. thesis, University of Adelaide, 2009.
[37] R. Aloisio and F. Tortorici, Astropart. Phys. **29**, 307 (2008).
[38] http://www.narrabri.atnf.csiro.au/observing/CABB.html.
[39] P. Roberts, Ionospheric Dispersion Compensation Using a Novel Microwave De-dispersion Filter, Workshop on App. of Radio Sci. (WARS), Gold Coast, Australia, 2008, http://www.ncrs.org.au/wars/wars2008/Roberts\%20WARS\%202008.pdf.
[40] Crustal Dynamics Data Information System (CDDIS), NASA, 2007, http://cddisa.gsfc.nasa.gov/gnss_datasum.html.
[41] R. A. McFadden, R. D. Ekers, C. W. James, D. Jones, P. Roberts, and R. J. Protheroe, *30th ICRC, Merida, Mexico, 2007*; arXiv:0801.3304v1.
[42] J. Álvarez-Muñiz and E. Zas, Phys. Lett. B **434**, 396 (1998).
[43] N. G. Lehtinen, P. W. Gorham, A. R. Jacobsen, and R. A. Roussel-Dupré, Phys. Rev. D **69**, 013008 (2004).
[44] National Geodetic Survey web site: www.ngs.noaa.gov/orbits/.
[45] D. R. Williams, Dissertation, University of California, 2004.
[46] V. S. Troitskij and T. V. Tikhonova, Izv. Vyssh. Uchebn. Zaved., Radiofiz. **13**, 1272 (1970).
[47] M. H. Wieringa and M. J. Kesteven, Measurements of the ATCA primary beam, ATNF Technical Memo Series,

d96b7e1, 1992.
[48] I. Kravchenko *et al.*, Phys. Rev. D **73**, 082002 (2006).
[49] P. Gorham *et al.*, Phys. Rev. Lett. **103**, 051103 (2009).
[50] R. Gandhi, C. Quigg, M. H. Reno, and I. Sarcevic, Phys. Rev. D **58**, 093009 (1998).
[51] A. Cooper-Sarkar and S. Sarkar, J. High Energy Phys. 01 (2008) 075.
[52] M. Griswold, M. Harrison, and D. Saltzberg, J. Opt. Soc. Am. A **24**, 3207 (2007).
[53] J. Álvarez-Muñiz and E. Zas, Phys. Lett. B **411**, 218 (1997).
[54] G. Olhoeft and D. Strangway, Earth Planet. Sci. Lett. **24**, 394 (1975).
[55] A. Ishihara (IceCube Collaboration), arXiv:0711.0353v1.
[56] J. Abraham *et al.* (The Pierre Auger Collaboration), Phys. Rev. D **79**, 102001 (2009).